Title
Tunable diode laser measurements of formaldehyde during the TOPSE 2000 study: Distributions, trends, and model comparisons

Journal
Journal of Geophysical Research, 108(D4)

ISSN
0148-0227

Authors
Fried, Alan
Wang, Yuhang
Cantrell, Chris
et al.

Publication Date
2003

DOI
10.1029/2002jd002208

Tunable diode laser measurements of formaldehyde during the TOPSE 2000 study: Distributions, trends, and model comparisons

Alan Fried,[1] Yuhang Wang,[2,3] Chris Cantrell,[1] Bryan Wert,[1,4] James Walega,[1] Brian Ridley,[1] Elliot Atlas,[1] Rick Shetter,[1] Barry Lefer,[1] M. T. Coffey,[1] Jim Hannigan,[1] Donald Blake,[5] Nicola Blake,[5] Simone Meinardi,[5] Bob Talbot,[6] Jack Dibb,[6] Eric Scheuer,[6] Oliver Wingenter,[7] Julie Snow,[8] Brian Heikes,[8] and Dieter Ehhalt[9]

Received 16 February 2002; revised 30 April 2002; accepted 12 June 2002; published 13 February 2003.

[1] Airborne measurements of formaldehyde (CH_2O) were acquired employing tunable diode laser absorption spectroscopy (TDLAS) during the 2000 Tropospheric Ozone Production About the Spring Equinox (TOPSE) study. This study consisted of seven deployments spanning the time period from 4 February to 23 May 2000 and covered a wide latitudinal band from 40°N to 85°N. The median measured CH_2O concentrations, with a few exceptions, did not show any clear temporal trends from February to May in each of five altitude and three latitude bins examined. Detailed measurement–model comparisons were carried out using a variety of approaches employing two different steady state models. Because recent emissions of CH_2O and/or its precursors often result in model underpredictions, background conditions were identified using a number of chemical tracers. For background conditions at temperatures warmer than −45°C, the measurement–model agreement on average ranged between −13% and +5% (measurement–model/measurement), which corresponded to mean and median (measurement–model) differences of 3 ± 69 and −6 parts per trillion by volume (pptv), respectively. At very low temperatures starting at around −45°C, significant and persistent (measurement–model) differences were observed from February to early April from southern Canada to the Arctic Ocean in the 6–8 km altitude range. In such cases, measured CH_2O was as much as 392 pptv higher than modeled, and the median difference was 132 pptv (83%). Low light conditions as well as cold temperatures may be important in this effect. A number of possible mechanisms involving the reaction of CH_3O_2 with HO_2 to produce CH_2O directly were investigated, but in each case the discrepancy was only minimally reduced. Other possibilities were also considered but in each case there was no compelling evidence to support any of the hypotheses. Whatever the cause, the elevated CH_2O concentrations significantly impact upper tropospheric HO_x levels at high latitudes (>57°N) in the February–April time frame. *INDEX TERMS:* 0365 Atmospheric Composition and Structure: Troposphere—composition and chemistry; 0368 Atmospheric Composition and Structure: Troposphere—constituent transport chemistry; 0394 Atmospheric Composition and Structure: Instruments and techniques; *KEYWORDS:* airborne formaldehyde measurements, tunable diode laser measurements, formaldehyde measurements at high latitudes, formaldehyde during TOPSE

Citation: Fried, A., et al., Tunable diode laser measurements of formaldehyde during the TOPSE 2000 study: Distributions, trends, and model comparisons, *J. Geophys. Res.*, *108*(D4), 8365, doi:10.1029/2002JD002208, 2003.

[1]Atmospheric Chemistry Division, National Center for Atmospheric Research, Boulder, Colorado, USA.
[2]Department of Environmental Sciences, Rutgers University, New Brunswick, New Jersey, USA.
[3]Now at Earth and Atmospheric Sciences Department, Georgia Institute of Technology, Atlanta, Georgia, USA.
[4]Chemistry Department, University of Colorado, Boulder, Colorado, USA.
[5]Department of Chemistry, University of California, Irvine, Irvine, California, USA.
[6]Institute for the Study of Earth, Oceans, and Space, University of New Hampshire, Durham, New Hampshire, USA.
[7]Department of Chemistry, New Mexico Institute of Mining and Technology, Socorro, New Mexico, USA.
[8]School of Oceanography, University of Rhode Island, Narragansett, Rhode Island, USA.
[9]Institute for Atmospheric Chemistry, Julich, Germany.

0148-0227/03/2002JD002208

1. Introduction

[2] Over the past several years, there has been a great deal of interest in the chemistry and distributions of formaldehyde (CH_2O), an important reactive intermediate formed by the oxidation of many anthropogenic and biogenic hydrocarbons [e.g., *Sumner et al.*, 2002; *Weller et al.*, 2000; *Arlander et al.*, 1995; *Fried et al.*, 2002; *Frost et al.*, 2002, and references therein]. In addition to its reaction with OH (R1), CH_2O decomposes via two different photolysis channels ((R2a) and (R2b)), which depend upon wavelength [*Calvert et al.*, 2000].

$$\text{(R1)} \qquad CH_2O + OH \rightarrow HCO + H_2O$$

$$\text{(R2a)} \qquad CH_2O + h\nu(\lambda < 337\ \text{nm}) \rightarrow HCO + H$$

$$\text{(R2b)} \qquad CH_2O + h\nu(\lambda < 365\ \text{nm}) \rightarrow H_2 + CO$$

In the lower atmosphere, the radical products HCO and H generate the hydroperoxy radical HO_2 via (R3) and (R4):

$$\text{(R3)} \qquad HCO + O_2 \rightarrow HO_2 + CO$$

$$\text{(R4)} \qquad H + O_2 + M(N_2, O_2) \rightarrow HO_2 + M(N_2, O_2)$$

The radical photolysis channel (R2a) followed by (R3) and (R4) is a net source of odd hydrogen radicals, HO_x, (HO_x = HO_2 + OH + H) in the atmosphere. This radical channel takes on greater importance during high solar zenith angles [*Fried et al.*, 1997b] and in the middle to upper troposphere where radical production from $O(^1D)$ with H_2O diminishes as the available H_2O vapor decreases with altitude [*Wennberg et al.*, 1998]. In the study by *Fried et al.* [2002] during the 1997 North Atlantic Regional Experiment (NARE-97), for example, the radical photolysis channel of CH_2O comprises 34% of the total HO_x production rate between 4 and 8 km. This increases to 45% when only dry air in this altitude range was considered.

[3] The model results during NARE-97 were systematically lower than measurements by factors of 2–3. Despite the fact that altitudes higher than 8 km could not be studied during NARE-97, it is quite possible that elevated CH_2O concentrations could also be responsible, at least in part, for model underestimations of HO_x sometimes observed in the upper troposphere [*Wennberg et al.*, 1998; *Jaeglé et al.*, 1997, 1998, 2000; *McKeen et al.*, 1997; *Brune et al.*, 1998]. While the role of CH_2O has received some consideration in this regard, a number of investigators have proposed the importance of convective transport of peroxides [*Prather and Jacob*, 1997; *Jaeglé et al.*, 1997, 1998], as well as acetone photolysis, as the source of additional HO_x. However, based on NASA's Pacific Exploratory Missions (PEM), *Crawford et al.* [1999] raise the possibility that additional upper tropospheric HO_x sources are still needed.

[4] CH_2O is also important in other atmospheric regimes. In the relatively dry arctic boundary layer, CH_2O serves as both an important source of HO_x radicals and a sink for Br atoms; CH_2O competes with O_3 for the available Br [*de Serves*, 1994; *Shepson et al.*, 1996; *Sumner and Shepson*, 1999; *Sumner et al.*, 2002; *Ridley et al.*, 2003]. *Sumner et al.* [2002] and *Sumner and Shepson* [1999] have also found that CH_2O is emitted from the snowpack after polar sunrise, and in the absence of halogen atom chemistry the CH_2O concentration is often 200 parts per trillion by volume (pptv) or higher.

[5] As many hydrocarbon reactions initiated by OH, O_3, and/or Cl involve CH_2O as an intermediate, CH_2O becomes important in further testing our current understanding of hydrocarbon oxidation mechanisms as well as the consistency with the input OH concentrations employed in the models. According to *Crawford et al.* [1999], CH_2O is an ideal candidate for testing the presence of additional HO_x sources in the tropical upper troposphere. Unfortunately, measurement–model comparisons, even for remote background conditions where CH_4 oxidation is the primary CH_2O precursor, have exhibited both positive and negative deviations. However, many recent comparisons, including the NARE-97 study [*Frost et al.*, 2002], reveal model results that are systematically lower than measurements by factors of 2–3. The reader is referred to the studies of *Fried et al.* [2002] and *Frost et al.* [2002] for a comprehensive discussion of these comparisons. These discrepancies clearly point to gaps in our understanding of CH_2O production and destruction pathways in the clean background atmosphere, and perhaps unresolved measurement issues as well.

[6] Because of its importance, it is essential to acquire additional airborne measurements of CH_2O over a wide range of altitudes, latitudes, and photochemical conditions. It is also essential to follow up such measurements with model comparisons. The 2000 Tropospheric Ozone Production About the Spring Equinox (TOPSE) study presented such an opportunity. This campaign employed the National Center for Atmospheric Research's (NCAR) C-130 aircraft [*Atlas et al.*, 2003], which was configured to measure a suite of important atmospheric gases and particles. TOPSE consisted of seven deployments, spanning the time period from 4 February to 23 May 2000, and covered a wide latitudinal band from 40°N to 85°N.

[7] TOPSE provided a unique opportunity to study CH_2O photochemistry at northern middle to high latitudes during the winter-to-spring transition where the lifetime changes from several days to hours. On a few occasions during the early deployments the lifetime was as long as 1 month. This in turn allows us to extend our airborne measurement–model comparisons to a relatively new set of conditions not extensively studied. With the exception of a few flights during the 1997 SONEX [*Jaeglé et al.*, 2000] and the 1991 TROPOZ II [*Arlander et al.*, 1995] campaigns, to our knowledge there have been no airborne measurements of CH_2O at high latitudes.

2. CH_2O Measurements During TOPSE

2.1. Tunable Diode Laser Absorption Spectrometer (TDLAS) and Data Acquisition

[8] Based upon the lessons learned from earlier TDLAS systems, numerous modifications and improvements have been implemented for the TOPSE study. Comprehensive details regarding the forerunner systems for both ground-based and airborne measurements of CH_2O, calibration and sampling approaches employed, measurement accuracy and inlet tests, ground-based and airborne comparison studies, and absorption features utilized can be found in the studies of

Wert et al. [1996, 2002], *Fried et al.* [1996, 1997a, 1998a, 1998b, 1999, 2002], and *Gilpin et al.* [1997]. Specific details regarding the modified TDLAS employed during TOPSE can be found in the studies of *Wert et al.* [1999] and B. P. Wert et al. (Design and performance of a tunable diode laser absorption spectrometer for airborne formaldehyde measurements, submitted to *Journal of Geophysical Research*, 2003), and only a brief discussion will be presented here.

[9] The IR radiation from a liquid nitrogen cooled lead salt diode laser was directed through a multipass astigmatic Herriott cell (Aerodyne Incorporated) using a series of off-axis mirrors (2 parabolic and 1 elliptical mirror). The IR beam, which traces out a Lissajous pattern in the cell, achieves a total optical path length of 100 m in a 3-L sampling volume. Upon exiting the cell, the IR beam was directed onto sample and reference indium–antimonide photovoltaic detectors. The entire optical enclosure, including the optical bench, was temperature stabilized to 30°C, and this temperature control dramatically improved instrument performance. Data were acquired using second harmonic detection coupled with sweep integration, as discussed by *Fried et al.* [1998a].

[10] The inlet was comprised of multiple sections of 1.3 cm OD (0.95 cm ID) PFA Teflon line. Approximately 38 cm of the inlet, which protruded outside the aircraft and faced toward the rear of the airplane, was mounted within a winglet structure. The multiple inlet sections, from the inlet tip to the Herriott cell, were individually heated and controlled to temperatures between 30°C and 35°C. The inlet was heated to within 1.3 cm of the entrance tip. An addition port, located approximately 18 cm from the inlet tip, provided a means to add zero air to nearly the entire inlet upstream of the sampling cell. The inlet line also contained a standard addition port. The inlet section connected to an MKS 640A pressure controller mounted in the aircraft cabin about 53 cm downstream of the inlet tip and ultimately to the Herriott cell through 290 cm of the 1.3 cm OD PFA Teflon line. Ambient air was sampled by drawing airflow through this entire inlet (volume 0.24 L) and the Herriott cell by a vacuum pump. Employing sampling pressures around 40 torr, sample flow rates between 8.5 and 10 standard L min^{-1} (slm, where standard conditions are defined as 273 K and 760 torr), one calculates a sample residence time between 1.5 and 1.2 s.

[11] Zero air, generated by employing a second inlet using a diaphragm pump and a heated Pd/Al_2O_3 scrubber, was used to acquire background spectra. This scrubbing system removes CH_2O without significantly affecting the ambient water vapor concentration. During background acquisition, the zero airflow was rerouted into the inlet at flow rates exceeding the sample flow. As discussed by *Fried et al.* [1998a, 1998b], background spectra were acquired approximately twice every 1-1/2 min, and this approach very effectively captures and removes optical noise as well as the effects of sample line outgassing. *Wert et al.* [2002], based on extensive laboratory tests, have verified the sampling accuracy using this inlet under temperature, pressure, and relative humidity conditions indicative of the lower to middle troposphere.

[12] For calibration purposes, standards were generated using a pressure controlled CH_2O permeation system, the output of which was periodically added to zero air in the main inlet line. The calibration system contained two different permeation devices with different emission rates housed in separate glass chambers in a temperature controlled (70°C) aluminum block. At the cell flows employed, typical CH_2O standard concentrations of 12–14 ppbv were generated at the cell entrance. The CH_2O emissions rates were determined by comparisons with two other permeation devices, which in turn were verified employing a variety of techniques [*Fried et al.*, 1997a, 2002; *Gilpin et al.*, 1997]. These other devices were mounted in a laboratory-based calibration system that (1) did not leave the laboratory during the TOPSE campaign and (2) were maintained at temperature and had continuous airflow over the devices. Comparisons of both airborne standards with these two laboratory devices before and after TOPSE and with one another throughout TOPSE indicated that the emission rates of the airborne standards were constant to within 2%. Based upon the collective calibrations, we estimate a total calibration uncertainty of ±6% at the 1σ level for both permeation devices.

[13] During airborne operation, TDLAS measurements of CH_2O were typically acquired by averaging six successive 10-s ambient samples. Background spectra were acquired for 10 s before and after each 1-min ambient block using an appropriate delay period of 9 s (approximately 5 inlet/cell e-folding times) after each switch. The backgrounds surrounding each 1-min ambient block were averaged (time weighted) and subtracted point-by-point from the ambient spectrum. After applying a laser power correction, determined with each 1-min ambient block, each background-subtracted ambient spectrum was fit in real time to a background-subtracted calibration spectrum acquired previously employing a multiple linear regression approach [*Sewell et al.*, 1993]. Typically, the ambient flush background acquisition sequence was repeated for 30–60 min before a new calibration spectrum was acquired. Approximately 1–3 times a flight, a series of low emission rate CH_2O standards ($\approx$7 ppbv at the cell entrance) were added on top of ambient air, and after subtraction of the adjacent ambient spectra, processed in exactly the same manner as each sample spectrum. This procedure helped to ensure data quality by (1) identifying potential errors in the data acquisition/fitting retrieval procedures, (2) providing a direct measure of instrument precision through multiple calibrations, and (3) identifying the presence of sampling loss in the inlet line downstream of the zero air port. In all cases the retrieved CH_2O concentrations were within ±5% of the input values, and produced an average difference of ±1.3%. Each ambient acquisition cycle, which included the acquisition of a 10-s background, 1 min of ambient averaging, two 9-s delay periods and computer processing overhead, typically took 90 s. Henceforth we will refer to each ambient acquisition cycle so acquired as a 1-min average.

2.2. CH_2O Spectral Feature Employed

[14] The TDLAS measurements were carried out employing an isolated CH_2O absorption feature at 2831.6417 cm^{-1}. As discussed by *Fried et al.* [2002], this feature is clear of any known spectroscopic interferences with the exception of methanol. A weak methanol line approximately +0.009 cm^{-1} from the CH_2O feature has been measured in the laboratory by D. Richter (private communication, 2000). Laboratory tests indicate a positive interference of 3.8% on the retrieved CH_2O results. Ambient methanol concentra-

tions in the remote marine atmosphere typically fall within the 50–800 pptv range [*Singh et al.*, 1995; *Jaeglé et al.*, 2000], and thus methanol should on average produce a maximum interference of only +30 pptv on our ambient CH_2O values, and more typically around +15 pptv. During TOPSE, there were no continuous measurements of methanol; however, we make use of preliminary results from canisters for methanol acquired by the University of California, Irvine. Although these results are considered preliminary and further tests are needed to quantify the behavior of methanol in canisters, they do provide a rough estimate for correction of our CH_2O data. In most cases the percentage CH_2O correction is small; in 75% of the data where methanol values or interpolated values are available, the percentage CH_2O correction (0.038 * [methanol]/[CH_2O]meas) is $\leq$38%. The median methanol and CH_2O (uncorrected) concentrations for this group are 340 and 125 pptv, respectively. In terms of absolute values, the median correction is 14 pptv. Unless otherwise stated, all CH_2O measurements were corrected for methanol in this manner. Despite the above reassurances, one must still consider the possibility that the canister-derived methanol corrections may in some cases be too low, perhaps by as much as a factor of 2 (E. Apel, private communication, 2001). As will be shown in section 4, we consider this possibility in our measurement–model comparisons.

2.3. Measurement Precision and Accuracy Estimates

[15] It becomes important in measurement–model comparisons to accurately assess measurement precision and accuracy, particularly when examining such relationships at low mixing ratios less than 100 pptv. During TOPSE an upper limit to the measurement precision was estimated from the replicate precision upon sampling relatively constant ambient CH_2O levels. Numerous such time periods were identified during each flight, and all acquired ambient measurements close to these time periods were assigned the constant precision thus determined. These results were corroborated by periodic replicate precision measurements employing low-level standards and/or backgrounds. For the entire TOPSE campaign the 1-min measurement precision thus determined (1σ level) produced a median value of 40 pptv and an average of 44 $\pm$ 17 pptv.

[16] The systematic uncertainty was estimated from the above calibration uncertainty (6%) together with other systematic source estimates. Quadrature addition yields an estimated 1σ systematic uncertainty of $\pm$6.4% of the ambient concentration. This analysis does not include the methanol correction uncertainty since this uncertainty is not presently known. The systematic values thus determined were added in quadrature to the precision estimates discussed above to arrive at a total 1σ uncertainty for each 1-min average.

3. CH_2O Box Model Calculations

[17] Two different box models were employed in this study: a diurnal steady state box model similar to that previously used by *Davis et al.* [1996, 2001] and by *Crawford et al.* [1997, 1999] and further described by *Wang et al.* [2003], and a radical steady state model described by *Cantrell et al.* [2003]. Both models employed the same base chemical mechanisms and reaction rates, but differed in the method of solution, the method by which missing data, in particular nonmethane hydrocarbons (NMHCs), were interpolated between canister samples, and the method by which photolysis frequencies were incorporated. Most of the measurement–model comparisons that will be discussed in this paper, unless otherwise stated, are based on the diurnal steady state calculations. However, results in many cases are also presented using the radical steady state model because of its facility in allowing tests of various CH_2O production mechanisms. Both model calculations were carried out for every 1-min measurement period where measured peroxide data and NMHC and/or interpolated NMHC data were available.

3.1. Diurnal Steady State Box Model

[18] The model includes basic HO_x–NO_x–CH_4 gas phase chemistry along with NMHC chemistry, photolysis reactions, but no heterogeneous loss for soluble species. Reactions and rate coefficients were taken from *DeMore et al.* [1997] and *Atkinson et al.* [1997]. Photolysis rate coefficients were based on the DISORT four-stream NCAR Tropospheric Ultraviolet Visible (TUV) radiative transfer code (S. Madronich, http://www.acd.ucar.edu/TUV). Model calculations were constrained by observations of O_3, NO, CO, NMHCs, H_2O_2, CH_3OOH, temperature, water vapor, $J(O^1D)$, and $J(NO_2)$. Acetone was not measured and substantially more CO data were measured than NMHCs. Acetone and missing NMHC concentrations were scaled to observed CO [*Wang et al.*, 2003]. All model parameters except NO, NO_2, and photolysis rates, which were allowed to vary diurnally, were held constant in multiple-day runs. The concentrations of NO_x (NO + NO_2) were held at constant values that gave the observed NO concentrations at the time of the observation. The model calculated concentrations were reported when the diurnal cycles of such concentrations did not vary from day to day.

3.2. Radical Steady State Model

[19] A simple numerical model was constructed based on the assumption of photochemical steady state for each member of the HO_x and RO_x (CH_3O_2 plus higher organic peroxy radicals) family [*Cantrell et al.*, 1996, 2003]. A steady state equation was derived for each peroxy radical corresponding to a measured organic compound. Thus, concentrations were derived for OH, HO_2, and each of the respective RO_2 (including CH_3O_2) radicals. Steady state calculations of reservoir species were calculated separately using the same assumptions. The mechanisms and rate constant employed are given by [*Cantrell et al.*, 2003].

[20] In contrast to the diurnal steady state model, instantaneous photolysis frequencies are employed in the radical steady state calculations instead of time-integrated values. However, CH_2O box model calculations run with both types of photolysis frequencies yield a regression fit with a slope of 0.97. There was no indication of any seasonal trend in this agreement. As in the diurnal steady state model calculations, time periods where there were missing NMHC canister data had to be inferred. The radical steady state model employed the results from the previous canister measurements for this purpose.

[21] A Monte Carlo approach [*Cantrell et al.*, 2003] was used to estimate errors in the calculated CH_2O concentrations due to uncertainties in rate coefficients [*DeMore et al.*, 1997;

Sander et al., 2000] and measured concentrations of quantities used to constrain the equations. This results in a total 1σ uncertainty of about 34% in the calculated CH_2O concentrations, assuming all reactions are known. Since these uncertainties are common to both models, we have assumed an identical uncertainty for the diurnal steady state results.

3.3. Model Comparisons and Limitations

[22] Over the entire TOPSE data set the two modeling approaches produced results that agreed to within ±4% with an r^2 value of 0.94. The diurnal steady state model, moreover, was also run using input data from the NARE-97 campaign, and produced the NARE-97 box model results [*Frost et al.*, 2002] to within 7%. This eliminates model differences when assessing measurement–model comparisons between TOPSE and NARE-97.

[23] It is important to recognize the limitations of both models employed in this study. First, the veracity of both models depends upon the validity of the steady state assumption, and during TOPSE where the lifetime of CH_2O varies from a few hours to several days or more, the steady state assumption can easily become invalid. This will be particularly true during low light conditions where one encounters recent inputs of CH_2O and/or its precursors. Thus, one would expect that under most circumstances the steady state model validity would progressively break down with increasing CH_2O concentration, unless one is close to a source of CH_2O and/or its precursors. As shown by *Crawford et al.* [1999], enhanced CH_2O above steady state by a factor of 2 can be present at altitudes of 8–12 km at the end of 2 days after CH_3OOH, one of the precursors of CH_2O, is convectively pumped from the marine boundary layer. Although this represents an extreme set of conditions in the tropics, it serves to emphasize that the steady state CH_2O validity can be dictated by temporal variations of longer-lived precursors. In addition, the CH_2O production rate is very dependent upon the NO concentration, which influences the production rate for RO radicals ($NO + RO_2 = NO_2 + RO$), which in turn react with O_2 to produce CH_2O. Steady state calculations indicate that a factor of 2 change in NO changes CH_2O by a factor of 2 for the conditions prevalent during TOPSE. Thus, one would expect that the steady state assumption will readily break down under elevated and changing NO conditions. Secondly, since there are numerous NMHC precursors of CH_2O, there is the possibility that unmeasured NMHCs might become important in CH_2O production. Thirdly, the NMHCs that are measured might be misleading, particularly if they are highly reactive, such as alkenes. In these cases short-lived CH_2O precursors might have reacted away to form longer-lived CH_2O during the time between emission and sampling. In general, all three limitations will produce CH_2O model underestimations.

[24] Of course active CH_2O sinks not included in the box model will yield the reverse situation. In the midtroposphere, however, such sinks are generally not expected to be important. By contrast, both models are expected to have problems in the arctic boundary layer where CH_2O snowpack sources and Br sinks may become important [*Sumner et al.*, 2002; *Ridley et al.*, 2003]. Such periods, which constitute less than 0.5% of the measurement–model comparisons, have not been removed from the overall comparison data set but were removed from comparisons of background data discussed in section 5. In addition, both models do not include Cl chemistry, which may accelerate the production of CH_2O in certain cases, through the reaction of Cl with CH_4. Unfortunately there were no measurements of reactive Cl and/or Cl reservoir species on TOPSE, and thus no attempt was made to eliminate suspected Cl-influenced events. Finally, as the OH instrument during TOPSE experienced problems for altitudes above 3 km, the model calculations of the present study rely solely on modeled OH concentrations. Fortunately, an error in the calculated OH concentration does not have a large effect on the calculation of CH_2O, since OH is involved in both CH_2O production and destruction. For example, a factor of 2 change in OH, only changes the calculated steady state CH_2O concentration by ±26%.

4. CH_2O Distributions and Model Comparisons for the Entire TOPSE Data Set

4.1. CH_2O Distributions

[25] Measurements of CH_2O were acquired during all seven TOPSE deployments. During the fifth deployment, however, cell mirror reflectivity problems limited the number of useful CH_2O measurements, and those that are available are considerably less precise (1σ, 1-min precisions of 80–112 pptv) than the other measurements. Figure 1 shows the altitude dependence for all of the 1-min CH_2O measurements for three different latitude bins. The measurements in all cases were corrected for methanol interference, as previously discussed. Also shown are the median measured and modeled concentrations for five different altitude bins (0–0.2, 0.2–2, 2–4, 4–6, and 6–8 km). To facilitate discussion, we refer to the 3 latitude bins as midlatitude (40°–50°N), northern midlatitude (50°–57°N), and high latitude (>57°N). As can be seen, the midlatitude and northern midlatitude bins show the steepest altitude gradients in both measurements and modeled concentrations. This in part reflects the increased boundary layer sources, particularly during spring (to be shown in Figure 4), and the general tendency toward shorter CH_2O lifetimes at higher altitudes relative to the vertical mixing time. Table 1 tabulates CH_2O lifetimes by deployment, latitude, and altitude when ambient measurements were acquired. The midlatitude bin of Figure 1 exhibits the largest concentrations for all altitudes, as expected due to the closer proximity to sources. However, the high-latitude bin also shows reasonably high CH_2O concentrations, particularly the two highest altitude bins where some 1-min ambient levels reach 700 pptv (4–6 km) and 410 pptv (6–8 km).

[26] The median measured and modeled CH_2O concentrations for the midlatitude and northern midlatitude bins are generally in good agreement in Figure 1, while the high-latitude bin shows more pronounced discrepancies at all altitudes. This aspect will be examined in section 4.3. Table 2a further tabulates the measured and modeled values for each latitude–altitude bin, and Table 2b displays the corresponding differences.

4.2. Measurement–Model Comparisons

[27] Figure 2 displays a scatterplot for all 1-min CH_2O determinations acquired during TOPSE where corresponding modeled values were also available (N = 1959 points).

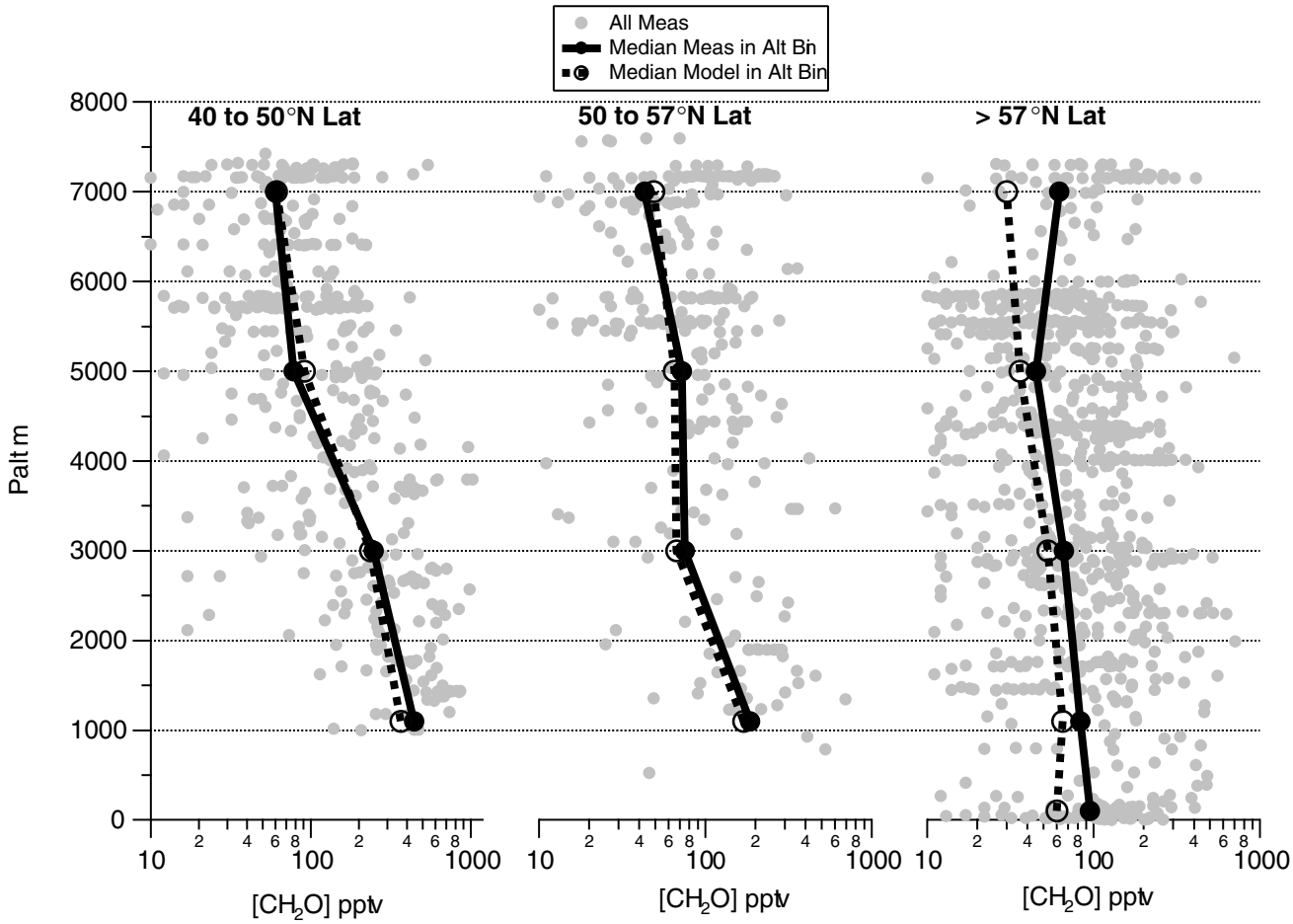

Figure 1. The altitude dependence of all 1-min CH_2O measurements (methanol corrected) acquired during TOPSE for three latitude bins. The median measured and base model (diurnal steady state model using modeled OH and HO_2 but measured peroxides) concentrations are given for five different altitude bins: 0–0.2, 0.2–2, 2–4, 4–6, and 6–8 km.

The modeled values were calculated using the base case model (i.e., diurnal steady state box model, using modeled OH and HO_2 concentrations, diurnally averaged photolysis frequencies, and measured concentrations for H_2O_2 and CH_3OOH). A linear regression of all the 1-min TOPSE data is shown. This and all subsequent linear regressions are based on weighted bivariate fits where the sum-squared perpendicular distances between each point and the fit line are minimized [*Neri et al.*, 1989], in contrast to a normal unweighted regression based on residual minimization of the ordinate values. As discussed by *Harder et al.* [1997], the results of the latter can be in error depending upon which variable is placed on the *x* and *y* axes. The bivariate fits were carried out with weights proportional to the reciprocal-squared total uncertainties for both the measurements and model calculations.

[28] The bivariate fit for all the TOPSE data of Figure 2 yields a slope of 1.08 ± 0.03 and an intercept of 7.2 ± 2.9 pptv, which is significantly different than the slope of 1.84 determined for NARE-97 [*Frost et al.*, 2002]. Although no methanol corrections were applied in the NARE study, the TOPSE slope without this correction (1.11 ± 0.03) is still considerably lower than NARE. Doubling the methanol correction, which assumes canister loss, produces a bivariate slope of 1.04 ± 0.03 and an intercept of −5.1 ± 2.9 pptv. Thus the regression results are not very sensitive to the methanol correction applied. Likewise these results are not very sensitive to whether or not measured or modeled peroxides (H_2O_2 and CH_3OOH) concentrations are used in the calculations. Employing modeled peroxide concentrations produces a slightly lower bivariate slope (1.04 ± 0.03) and higher intercept (12.1 ± 2.5 pptv). This is quite different than comparisons during the Mauna Loa studies [*Liu et al.*, 1992; *Zhou et al.*, 1996], where a difference in the calculated [CH_3OOH] as large as 330 pptv (700 pptv calculated by Liu et al. minus 370 pptv calculated by Zhou et al.) changed the calculated CH_2O concentration by 46% (95 pptv). During TOPSE the median calculated [CH_3OOH] is a factor of 2 lower than Mauna Loa, resulting in a reduced sensitivity to CH_3OOH.

[29] Despite the fact that the regression for all the TOPSE data indicates good measurement–model agreement on average, Figure 2 displays a number of points where the measurements are significantly different from the model values, and this is reflected in an r^2 value of 0.50. Also, one has to question the robustness of a linear fit where the majority of data (92% of the total) are concentrated between 0 and 300 pptv. If one arbitrarily restricts the regression to

Table 1. Calculated CH_2O Median Lifetimes in Hours as a Function of Deployment Number (D#) for Three Latitude and Five Altitude Bins[a]

Lat Bin	Palt Bin (km)	D1	D2	D3	D4	D6	D7
40–50°N	0–0.2	–	–	–	–	–	–
	0.2–2	66	5	4	7	3	2
	2–4	59	6	4	8	3	2
	4–6	187	4	3	4	2	2
	6–8	6	3	3	3	2	2
50–57°N	0–0.2	–	–	–	–	–	–
	0.2–2	8	4	3	5	3	3
	2–4	6	4	3	3	2	3
	4–6	6	4	3	2	3	3
	6–8	10	3	3	3	2	3
>57°N	0–0.2	16	72	4	10	4	4
	0.2–2	22	16	4	7	4	6
	2–4	20	12	4	6	5	3
	4–6	11	6	13	5	3	3
	6–8	16	11	6	4	3	2

[a]The calculations are based on calculated OH and instantaneous j-values ((R1), (R2a), and (R2b)) when ambient CH_2O measurements are present.

Table 2a. Tabulation of All 1-min CH_2O Measurements and Model Results When Both Are Simultaneously Present in Three Latitude and Five Altitude Bins for All Seven Deployments Combined[a]

Lat Bin	Palt Bin, km	Measurement Mean ± 1σ	Measurement Median	N	Model Median
40–50°N	0–0.2	–	–	–	–
	0.2–2	462 ± 206	441	44	364
	2–4	311 ± 262	247	108	235
	4–6	110 ± 119	78	198	91
	6–8	69 ± 82	60	142	61
50–57°N	0–0.2	–	–	–	–
	0.2–2	220 ± 147	185	34	170
	2–4	118 ± 137	75	39	67
	4–6	75 ± 74	72	133	65
	6–8	61 ± 84	43	154	49
>57°N	0–0.2	110 ± 96	95	71	60
	0.2–2	120 ± 138	83	137	65
	2–4	90 ± 110	66	259	53
	4–6	59 ± 80	45	519	36
	6–8	72 ± 89	62	121	30

[a]Measurements and model results are given in pptv. These results, which are further displayed in Figure 1, are not further parsed here for air mass type. N represents the number of points.

ordinate and abscissa <300 pptv, r^2 degrades to 0.13. Clearly a linear regression is less valid under these conditions since the combined uncertainty of both variables is similar to the data centroid. Finally, the model limitations previously discussed have not been eliminated for the full TOPSE data set of Figure 2. For example, many of the large discrepancies at model values >300 pptv correspond to low-altitude (1–4 km) measurements in the sixth and seventh deployments near Denver, CO. As discussed previously, such discrepancies reflect the inability to model local boundary layer sources. Table 2b reinforces this point; here the largest median (measurement–model) difference is observed at low altitudes in the lowest latitude bin. For these reasons it becomes important to look at the measurement–model comparisons using additional approaches.

[30] By averaging the measurements in 50 pptv model bins, we reduce the scatter significantly, thus facilitating the observation of trends. Of course this approach potentially obscures individual (measurement–model) differences, which may reflect real differences due to pertinent atmospheric processes. Figure 2 displays the bin averages along with the resulting bivariate fit up to model values $\leq$350 pptv. As can be seen, the regression slope changes from 1.08 for the full comparison to 1.14 ± 0.08 for the binned averages and r^2 increases to 0.97. This suggests that upon reducing the scatter, which at CH_2O < 200 pptv is to a large extent from measurement imprecision, one observes no overall systematic bias in the measurement–model comparison. Including the remaining 6 points above 350 pptv in the fit increases the slope to 1.19 and decreases r^2 to 0.89. However, as can be seen by the dashed line, which extrapolates the 7-point linear fit out to model values of 700 pptv, the linear measurement–model fit is no longer adequate starting at model values around 350 pptv (measured values $\approx$400 pptv). Many of these higher concentration points are influenced by local sources where the model limitations take on greater importance.

[31] It is also useful to look at histograms of the (measurement–model) differences for two different measurement regimes. Figure 3 displays such a histogram for the entire data set (solid black bars) as well as for a subset where measurements are less than 400 pptv (light gray bars). Based on mean and median measured CH_2O concentrations (when diurnal steady state calculations are present) of 105 and 68 pptv, respectively, one arrives at fractional differences (measurement–model/measurement) ranging between 12% and 23% for the entire TOPSE data set. Where there are no black bars showing in Figure 3, such as for many of the differences to the left of 0, all the measurements are less than 400 pptv. Conversely, where only black bars are shown, all the measurements are greater than 400 pptv. The 400 pptv measurement cutoff limit was chosen using the results of Figure 2. As can be seen, the largest differ-

Table 2b. Tabulation of All 1-min Point-to-Point CH_2O (Measurement–Model) Differences in Three Latitude and Five Altitude Bins for All Seven Deployments Combined[a]

Lat Bin	Palt Bin, km	Mean Diff. ± 1σ	Median Diff.	N	Diff. Range
40–50°N	0–0.2	–	–	–	–
	0.2–2	109 ± 176	111	44	−209 to 482
	2–4	47 ± 172	9	108	−289 to 634
	4–6	8 ± 100	4	198	−217 to 556
	6–8	−1 ± 82	−7	142	−209 to 434
50–57°N	0–0.2	–	–	–	–
	0.2–2	66 ± 130	22	34	110 to 434
	2–4	17 ± 196	4	39	−135 to 306
	4–6	7 ± 68	3	133	−124 to 272
	6–8	11 ± 87	−4	154	−129 to 276
>57°N	0–0.2	60 ± 88	52	71	−94 to 384
	0.2 − 2	49 ± 140	13	137	−174 to 602
	2–4	23 ± 87	10	259	−241 to 466
	4–6	17 ± 75	5	519	−120 to 670
	6 −8	42 ± 90	35	121	−94 to 391

[a]Differences (Diff.) are given in pptv. Note that the median point-to-point differences here are slightly different than the differences of the median values shown in Table 2a. N represents the number of points.

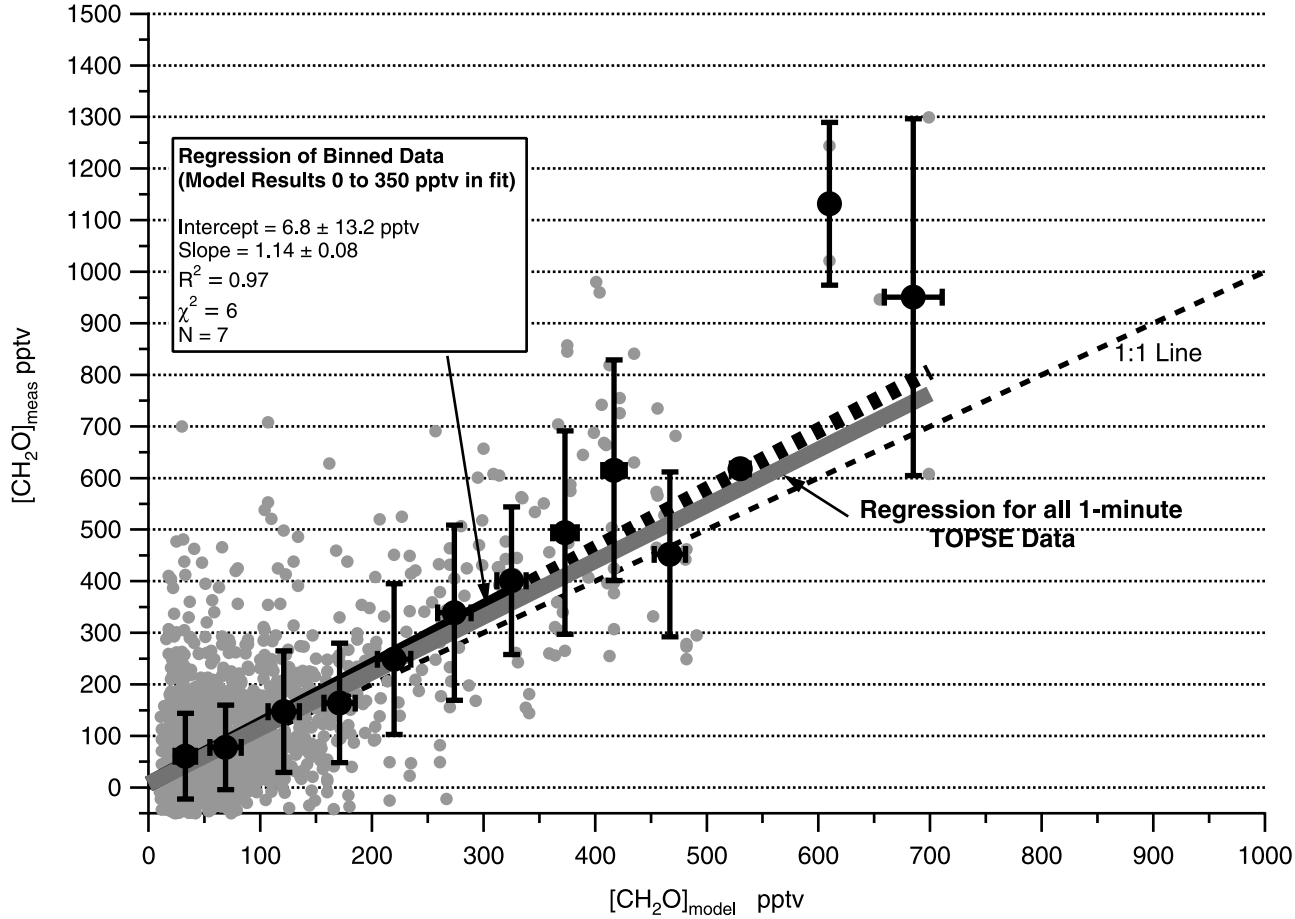

Figure 2. Scatterplot for all 1-min CH_2O determinations (lighter filled circles) versus base case model calculations. The dark filled circles represent the result of averaging the original data into 50 pptv model bins. The error bars represent the bin standard deviation.

ences are positive and these are almost exclusively comprised of measurements >400 pptv. Negligibly few differences less than 0 are associated with measurements >400 pptv. Thus the model tends to underestimate the measurements as the measured values increase, which is consistent with the model limitations discussed previously. Based on these limitations, one would expect to observe a correlation between (measurement–model) difference and CH_2O lifetime. Over 95% of the comparison points have instantaneous lifetimes $\leq$15 hours, and the resulting scatterplot of the (measurement–model) difference versus CH_2O lifetime reveals no correlation ($r^2 = 6 \times 10^{-6}$) and a slope of 0 within the uncertainty bounds. However, there is a correlation between model underprediction and evidence of fresh emissions; most of the large scatter in Figure 2 occurs when, for example, levels of CNC (>1000 particles cm^{-3}) and ethene are elevated (>7 pptv).

[32] The various analyses just presented for the entire TOPSE data set indicates an overall measurement–model agreement that on average falls within the 4–23% range. These analyses also indicate a number of comparison points with large (measurement–model) discrepancies, particularly for elevated ambient CH_2O concentrations. Of the 1959 comparisons for the full data set, 19% reveal (measurement–model) discrepancies greater than the total combined (2σ) measurement–model uncertainty for each point, calculated by quadrature addition of the uncertainties previously discussed. Such points will hereafter be designated as outliers.

4.3. Measured and Modeled [CH_2O] as a Function of Altitude and Deployment

[33] In Figures 4a–4c, the measured and modeled CH_2O results of Figure 1 are broken out into separate deployments for the five altitude bins where there are simultaneous measurements and model values, the number of which is denoted with each bin. Only the diurnal steady state model results are shown here; however, the radical steady state model yields very similar results.

[34] The measured CH_2O concentrations in the midlatitude bin display the steepest altitude gradients for all deployments; the median measured CH_2O levels fall within the 300–450 pptv range for the 0.2–2 km altitude range for all but the last deployment and this drops off to levels primarily in the 50–60 pptv range for all time periods in the 6–8 km altitude bin. The low-altitude observations reflect enhanced boundary layer sources of CH_2O and its precursors, particularly in the spring, increased CH_2O production from increased OH and NO concentrations, and an enhanced OH + CH_4 reaction rate due to the elevated temperature relative to higher altitudes. By contrast, the midlatitude 6–8 km observations largely reflect methane oxidation and an increased destruction rate by photolysis and OH reaction.

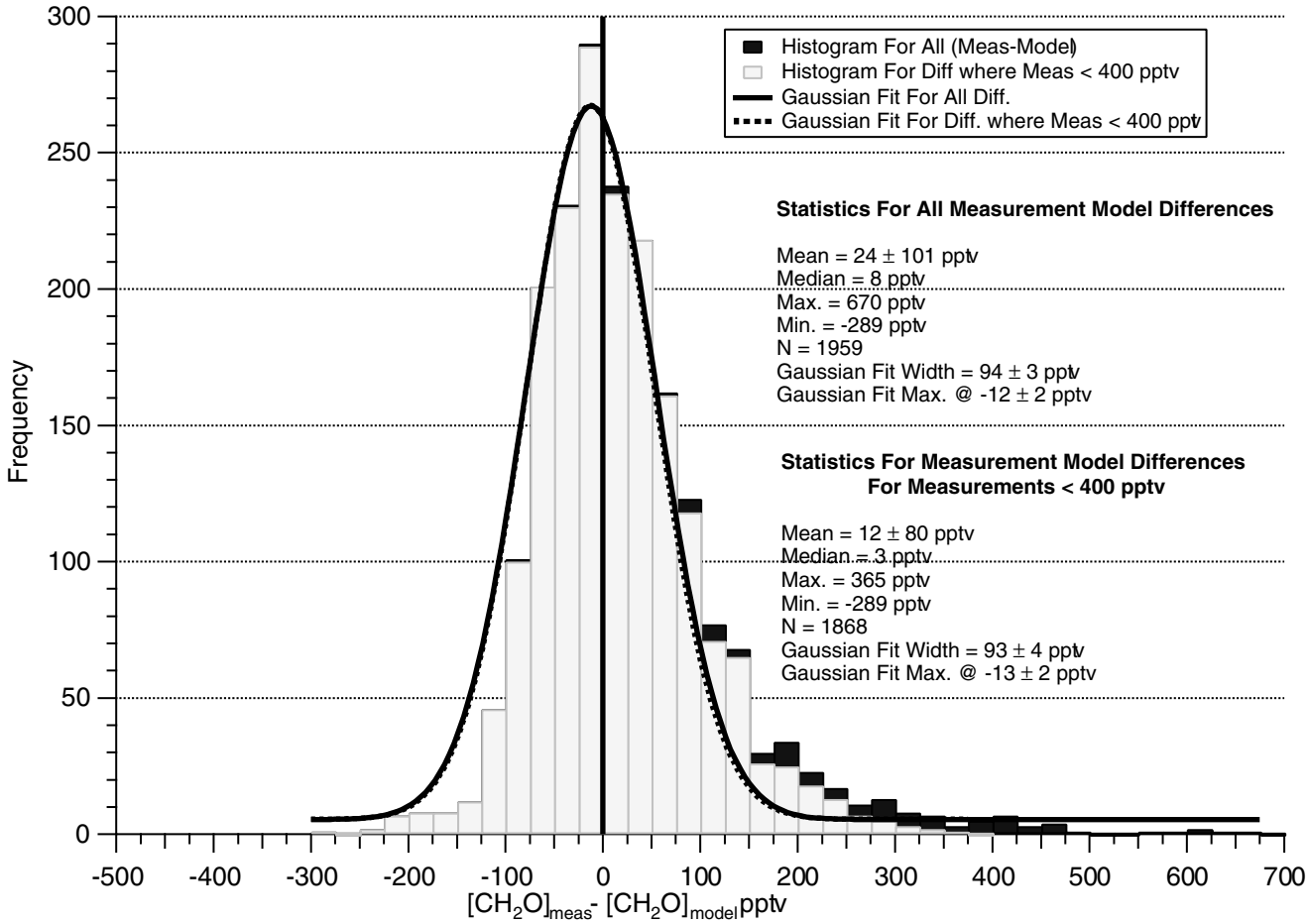

Figure 3. Histograms of the (measurement − base model) CH_2O difference for all the comparison points (solid black bars) and for the subset where $[CH_2O] < 400$ pptv (light gray bars). The Gaussian fit is shown for reference.

With the exception of the second and sixth deployments, the steep CH_2O gradients with altitude above are significantly reduced for the northern midlatitude and high-latitude bins, perhaps reflecting lower CH_2O boundary layer sources. The model altitude profiles of Figure 4 in many cases capture the same broad features as the measurements. However, in many cases there are also significant differences. In most such instances the model results are lower than the measurements, particularly at low altitudes where the measured CH_2O concentrations are high and thus the model limitations previously discussed may become prevalent. However, there are also cases of model underprediction for measurements <250 pptv. The 6–8 km high-latitude comparisons of the second to fourth deployments are particularly interesting in this regard: (1) the median point-by-point (measurement–model) differences are 129, 124, and 99 pptv for the second to fourth deployments, respectively, and these are significantly larger than all the 6–8 km high-latitude comparisons (median difference = 35 pptv); (2) the regimes in question comprise a nontrivial fraction (25%) of the 6–8 km high-latitude comparisons; and (3) the elevated CH_2O can give rise to elevated HO_x levels, as will be further discussed. The 3 high-altitude, high-latitude comparisons of the second deployment are further supported by an additional 18 comparisons based upon the radical steady state model (median difference = 181 pptv). The model also underpredicts the observations in the 4–6 km altitude bin for high latitudes during the second to fourth deployments.

[35] It is interesting to note that the high-latitude 4–8 km discrepancies just cited are no longer present in the sixth and seventh deployments, at least on a deployment-averaged basis. This fact illustrates the importance of explicitly examining the temporal dependence in the measurement–model comparisons, and this is shown in Figures 5 and 6. In Figure 5, we display the measured and (diurnal steady state) modeled CH_2O for the two highest altitude bins versus deployment number for all three latitude bins along with linear fits of these parameters versus time (slopes designated next to each line). Figure 6 shows this same plot for the next two lower-altitude bins. In Figure 5, the measured and modeled temporal profiles are negligibly small and nearly identical to one another (to within the slope uncertainties) for both the midlatitude and northern midlatitude bins in the 6–8 km altitude range. Although the scatter is significantly larger for the corresponding data in the 4–6 km range, again the measured and modeled temporal profiles are nearly identical to one another within and between each latitude bin. At high latitudes, the measurements in both altitude ranges of Figure 5 show significant departure from the behavior above. In contrast to the model profiles in both

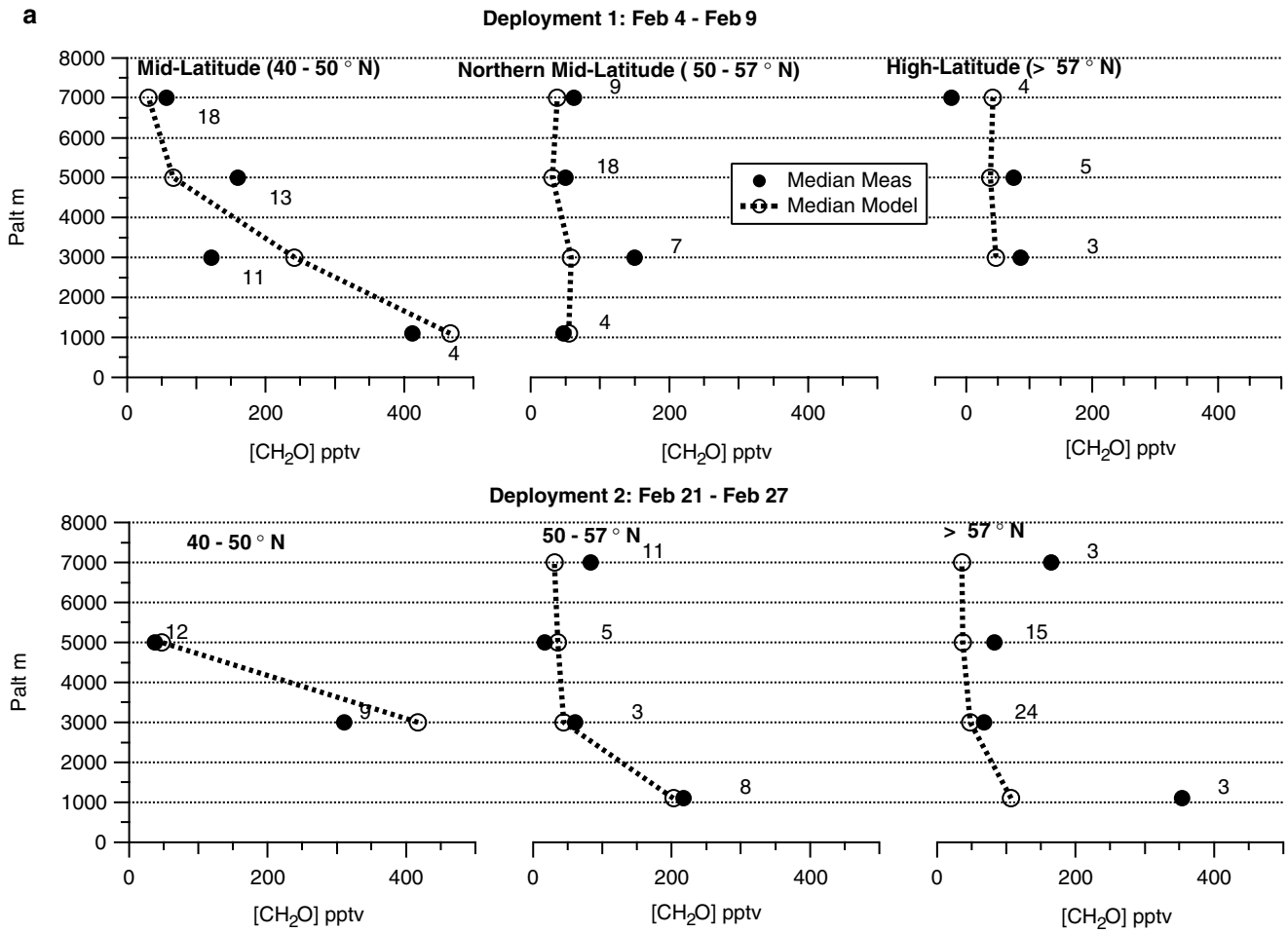

Figure 4. (a)–(c) Deployment altitude profiles for the median CH_2O measured (dark circles) and (base case) modeled (open circles) concentrations for three different latitude bins and the five altitudes bins of Figure 1. The number of comparison points is denoted with each altitude bin.

altitude ranges, where the values typically fall in the 20–40 pptv range with no discernable temporal trend, the measurements show a definite negative temporal dependence. This dependence is particularly pronounced for the 6–8 km altitude bin in deployments 2–7 (−28 pptv deployment^{-1}, −48 pptv month^{-1}). This negative trend in the 4–6 km range, although not as pronounced, is still present (−10 pptv deployment^{-1}, −17 pptv month^{-1}). It is worth noting that Figures 4 and 5 do not show these same observations for the first deployment, which in part reflects the limited number of (diurnal steady state) comparisons and in part the overall warmer ambient temperatures (to be discussed). However, additional comparisons using the radical steady state model (Table 3 to be discussed) show a median (measurement–model) difference of 162 pptv for the first deployment at ambient temperatures of −51.6°C, which is similar to that for the second deployment.

[36] In Figure 6, one observes higher measured and modeled CH_2O levels and associated higher scatter in the midlatitude bin compared to the northern midlatitude and high-latitude bins. However, there are no discernable differences (to within the slope uncertainties) in the measured and modeled trends within or between each bin. Table 3 tabulates all the high-altitude (6–8 km) and high-latitude (>57°N) measurement and model results and the associated sampling conditions. Each row in the table is comprised of a continuous time period within which there are measurement–model comparisons and which satisfy the altitude and latitude conditions above. Both the diurnal steady state and radical steady state measurement–model comparisons are shown. All of the diurnal steady state measurement–model comparisons of Table 3 are used in deriving the 6–8 km high-latitude results of Figure 5 and corresponding comparisons in Figures 4a–4c. Because of the input differences, the radical steady state model in some cases increases the number of measurement–model comparisons. For emphasis, rows in Table 3 with large (measurement–model) discrepancies are indicated in boldface. In all such cases exhibiting large discrepancies there are no signs of recent anthropogenic pollution; tracers like CO, NO, NO_x, CNC, and the sum of NMHC (which includes all the alkanes, cycloalkanes, alkenes, and alkynes measured in canisters, see *Blake et al.* [2003]) are indicative of background air (to be discussed). Comparisons on 7 and 24 March are influenced by the stratosphere. Thus, the elevated measured CH_2O levels and associated large (measurement–model)

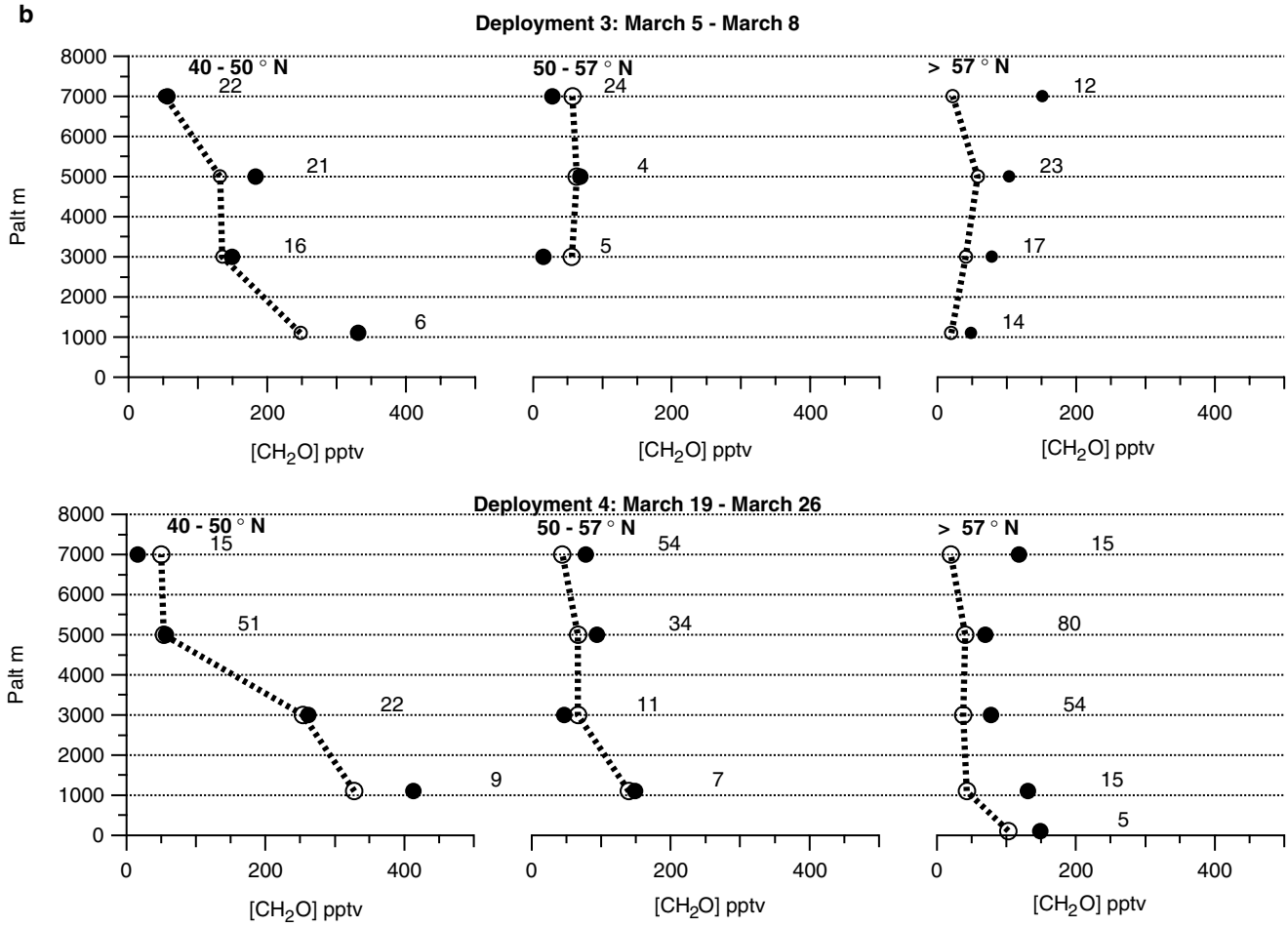

Figure 4. (continued)

discrepancies cannot be explained by fresh anthropogenic pollution. Moreover, the discrepancies of Table 3, as well as for other latitude and altitude bins, cannot be explained by measurement imprecision, as will now be discussed.

4.4. Measured and Modeled [CH_2O] Time Series for Two Different High-Altitude and High-Latitude Flight Legs

[37] It is important to examine the magnitude of the high-altitude (6–8 km), high-latitude (>57°N) discrepancies just noted relative to the total measurement and model uncertainties. In Figures 7a and 7b, we plot two time series comparisons acquired during deployments 3 (7 March, see Table 3) and 7 (18 May, see Table 3) to address this issue. These data constitute a subset of the high-altitude and high-latitude data shown in Figure 5. The locations for both time series are reasonably close (see Table 3). As can be seen in Figure 7a, the measurements, with a few exceptions, are substantially higher than both the diurnal steady state and the radical steady state model profiles, which are in excellent agreement. These differences are considerably larger than the total measurement and model uncertainties at the 2σ levels, which are shown by the error bars on each point. The dips in measured CH_2O at 1506 and 1519 GMT correspond to dips in measured CO, which suggests a change in air mass. The drop in measured CH_2O starting at 1539 GMT corresponds to an increase in ambient temperature; the temperature increases from a median value of −46°C for the 19 measurements prior to 1539 GMT to a median value of −43.9°C for the last 3 points in Figure 7a. As will be discussed, ambient temperature is an important factor in the (measurement–model) discrepancy. The median measured and modeled (diurnal steady state) CH_2O concentrations in Figure 7a are 151 and 22 pptv, respectively, and the median point-to-point (measurement–model) difference is 124 pptv. The corresponding median point-to-point difference using the radical steady state model is 129 pptv. Similar large discrepancies, which are greater than the combined known measurement–model uncertainties, are obtained for additional high-altitude, high-latitude time series profiles for deployments 2–4.

[38] In contrast to Figure 7a, Figure 7b yields measurement–model agreement within the combined uncertainties. With the exception of one point (around 1400 GMT), the measurements oscillate about both model results. The median measured and modeled (diurnal steady state) CH_2O concentrations are 20 and 30 pptv, respectively, and the median point-by-point (measurement–model) difference is −9 pptv. Similar results are obtained using the radical steady state model. Other high-altitude, high-latitude profiles throughout deployments 6 and 7 show similar behavior as Figure 7b. Figures 7a and 7b and related plots

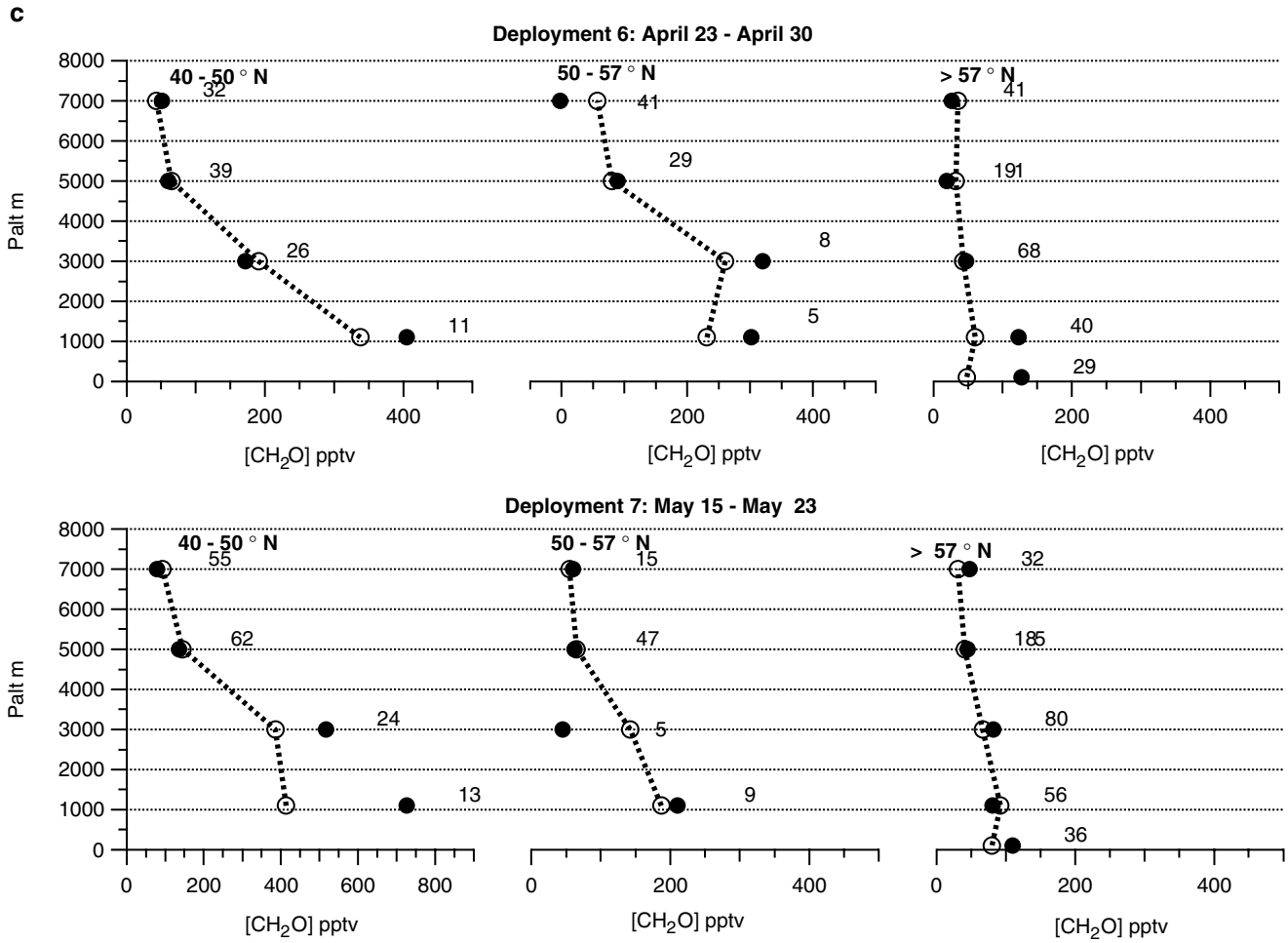

Figure 4. (continued)

provide evidence that the unique high-latitude temporal profile for the 6–8 km altitude range of Figure 5 is not caused by measurement imprecision nor measurement error, at least known error; numerous instrument status and housekeeping variables did not show any anomalies in the measurements. In addition, back trajectories for these as well as additional high-altitude and high-latitude legs show nothing very definitive regarding unique air mass origin to explain the differences in the two figures (i.e., differences in air mass regimes). In many cases the air passed over the same general region in northern Canada, north of the flight track, at altitudes between 6 and 9 km 2 days before sampling for both regimes. After 5 days, the air passed over the Arctic Ocean for both regimes. In other cases the air in both regimes originated from the same latitude as the flight track over the Gulf of Alaska.

5. CH_2O Distributions and Measurement–Model Comparisons for Background Conditions

5.1. Background Parsing Criteria

[39] Background conditions were identified using a number of tracers, which are tabulated in Table 4, to minimize the model shortcomings. As discussed in section 3.3 and further by *Frost et al.* [2002], recent emissions of NO_x (within a few days of sampling) from anthropogenic, biogenic, or lightning sources would result in model underprediction of CH_2O. Likewise elevated anthropogenic tracers like CO, C_2Cl_4, benzene, NMHCs, and elevated particles from CNC measurements were also used to eliminate the model shortcomings. The background cutoff limits were determined by plotting histograms for each species over the TOPSE campaign. With the exception of O_3, the upper 10% of each histogram defined the cutoff limits, above which the data were removed. In the case of O_3 no upper limit was defined since in many cases elevated O_3 is associated with stratospherically influenced air. The lower O_3 limit of 37 ppbv represents the lower 10% level, below which data were removed. This was set higher than the partial ozone depletion event (PODE) limit of 20 ppbv defined by *Ridley et al.* [2003] to further minimize snowpack emissions of CH_2O. According to *Sumner et al.* [2002], this source is inversely correlated with O_3, and the snowpack CH_2O concentration at the surface falls off to around 100 pptv at O_3 levels higher than ≈37 ppbv. Cutoff limits for the NMHC sum, the alkene sum, and CNC were set to the upper 20%, thus making the selection more stringent. Although even more stringent limits can be chosen at the expense of the number of comparison points, the collective limits of Table 4

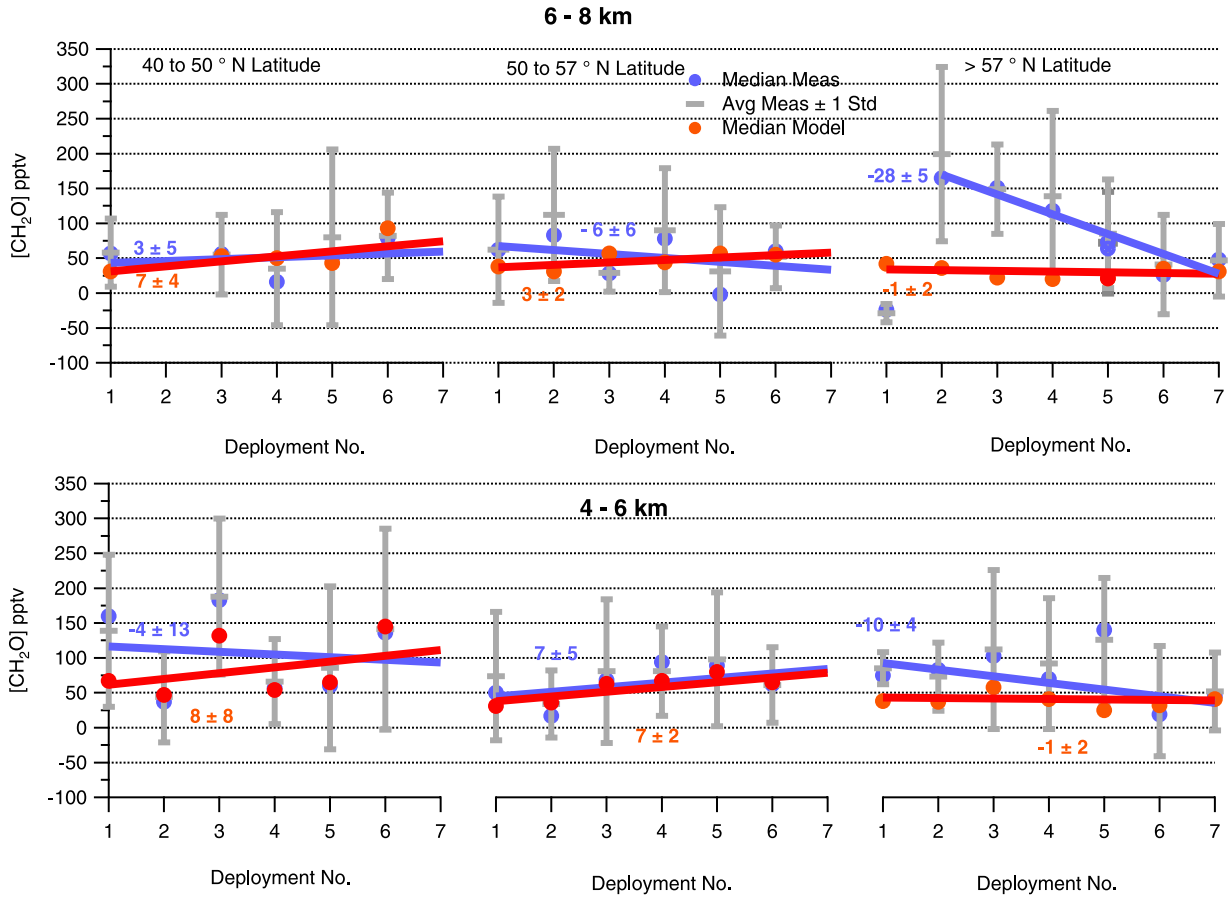

Figure 5. Median measured, (base case) modeled, and mean $[CH_2O] \pm 1\sigma$ for the two highest altitude bins and three latitude bins versus deployment number for the full TOPSE data set. Also shown is the linear fit for the median measured (solid blue line) and median modeled (solid red line) concentrations versus deployment. The numbers near each line designate the slope and standard deviation of the fit. Results for the fifth deployment are included for informational purposes but not included in the linear fits.

ensure that most of the air masses under study are well aged, devoid of fresh emissions.

5.2. Measurement–Model Comparisons and Distributions for Background Conditions

[40] Employing the selection criteria of Table 4, a total of 743 1-min measurement–model (diurnal steady state) comparisons points were identified for 6 deployments (eliminated deployment 5). The selection criteria based on the continuous measurements of NO, NO_x, NO_y, and CNC, pare down the 1959 points for the full data set to 1046, and the canister measurements of CO, and hydrocarbons remove an additional 303 points. In contrast to the full data set, the maximum measurement and model CH_2O values for background conditions defined in Table 4 are 481 and 242 pptv, respectively, and 99% of the measurements are less than 300 pptv. Table 5a tabulates the CH_2O measurement and model results for these background conditions for the three latitude and five altitude bands previously discussed, and Table 5b tabulates the point-to-point (measurement–model) differences. These tables are analogous to Tables 2a and 2b for the full TOPSE data set. Both data sets yield fairly similar results at high altitudes (4–8 km) in all 3 latitude regimes, but the full data set yields significantly higher mean and median results at lower altitudes.

[41] A histogram similar to Figure 3 can be constructed for the background data, and at temperatures warmer than −45°C (N = 711 points), this results in the following (measurement–model) differences: mean = 3 ± 69 pptv and median = −6 pptv. The slightly improved measurement–model agreement compared to the full data set are also reflected in the (measurement–model/measurement) fractional differences; the background data yields values of −13% to 5% compared 12–23% for the full data set. Figure 8 displays a slightly revised histogram for the background data. Here the (measurement–model) differences are ratioed to the combined 2σ measurement–model uncertainty limits on a point-by-point basis. The measurement uncertainty, which is dominated by measurement precision, in general exhibits a factor of 2 larger uncertainty than that from the model under background conditions. Thus, the uncertainty term of Figure 8 is largely governed by the measurement precision, and this is reflected in the near Gaussian profile (Gaussian fit denoted by dark solid line)

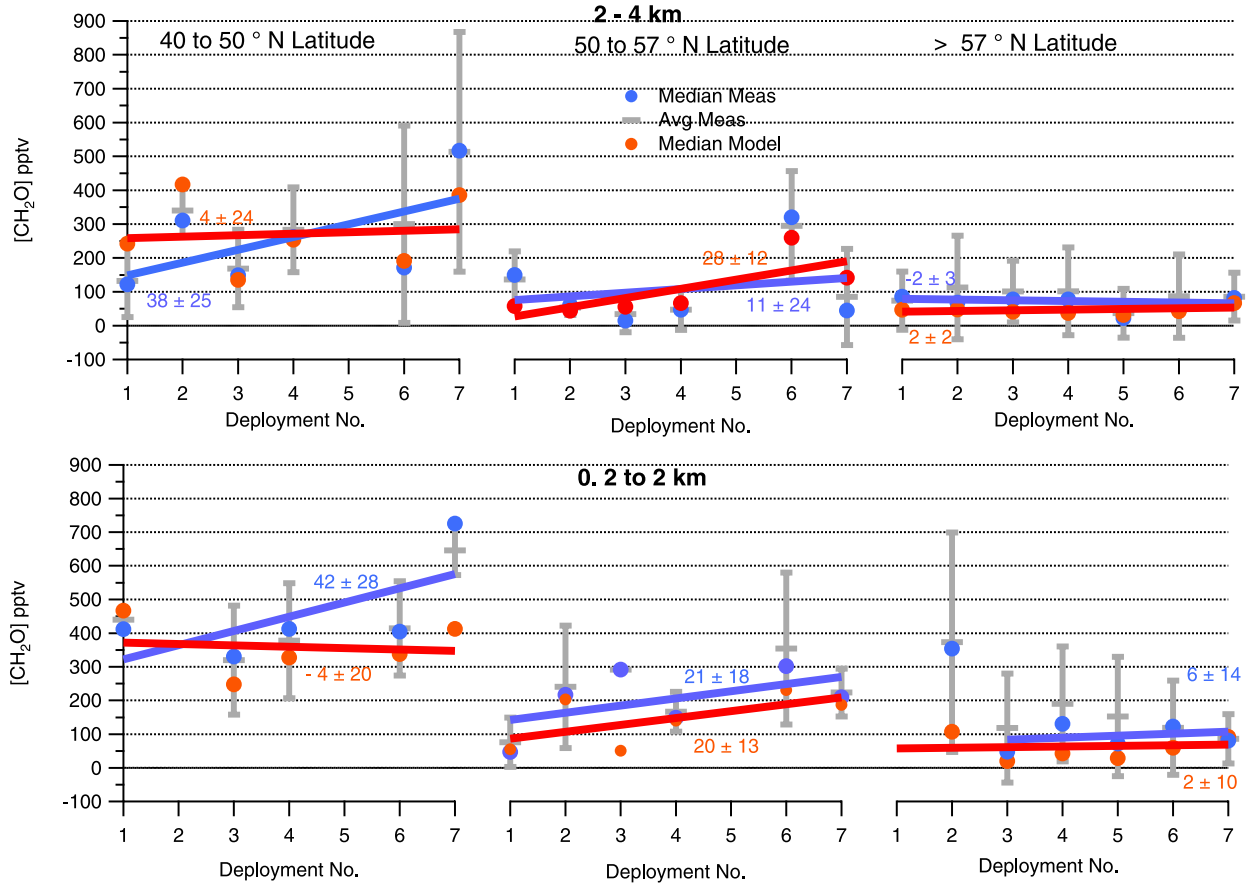

Figure 6. Identical to Figure 5 but only for the 2–4 and 0.2–2 km altitude bins.

for the normalized (measurement–model) difference. Comparison data larger than the combined uncertainty limits at the 2σ level, lie to the left and right of the dashed vertical lines at −1 and +1, respectively. Fourteen percent of the data fall in this region. While larger than 5% one would expect based on purely random and uncorrelated measurement and model uncertainties, the results of Figure 8 represent a slight improvement over the 19% value obtained for the full data set. The peak Gaussian fit value is centered near 0, which indicates near 0 measurement–model bias for the background data at temperatures warmer than −45°C.

[42] A bivariate regression fit of the background data where the measurements are averaged into 25 pptv model bins, results in the following: slope = 0.98 ± 0.14, intercept = −2.6 ± 8.4 pptv, and r^2 = 0.93. The slightly smaller slope compared to the binned regression for the full data set of Figure 2 (1.14) again reflects improved measurement–model agreement employing background conditions, which attempts to minimize the model shortcomings discussed previously. As in section 4.2, we considered the effect of doubling the methanol correction, which assumes canister loss. For background conditions, the mean and median (measurement–model) differences of Figure 8 are slightly increased to −12 ± 71 and −20 pptv, respectively. Since the resulting corrected ambient levels are so low (mean = 44 pptv and median = 34 pptv), these small absolute discrepancies translate to rather large percentage discrepancies of −27% to −59%. Doubling the methanol correction has no effect on the slope for the binned background data.

[43] The background comparisons thus far have been restricted to ambient sampling temperatures >−45°C. This, in conjunction with the fact that the NO_y selection limit of Table 4 eliminates some very interesting stratospherically influenced air masses, and the averages of Tables 5a and 5b mix in periods of good agreement with poor agreement, gives the false impression that the large (measurement–model) differences previously noted for the high-latitude and high-altitude bins are no longer present. On the contrary, these discrepancies are still present and reveal some very important mechanistic information about CH_2O production as a function of temperature.

6. Temperature Dependence of the Model Underprediction

[44] Table 6 lists the median deployment ambient temperature for each latitude bin for the two highest altitude ranges (4–6 and 6–8 km) for the entire TOPSE campaign when there are simultaneous CH_2O measurements (not parsed for clean background conditions) and model simulations. As can be seen, the highest latitude bin (>57°N) reveals the coldest sampling temperatures for each altitude range. The

Table 3. All the High-Altitude (6–8 km) and High-Latitude (>57°N) Measurement and Model Results for Each Deployment (D#) and the Associated Sampling Conditions[a]

D#	Steady State Model	Date	Time Start, GMT	Time Stop, GMT	Lat	Long	T	Meas	Model	N	Measurement–Model
1	**radical**	**Feb 7**	**1856:30**	**1859:30**	**66.4**	**−84.76**	**−51.6**	**173**	**11**	**2**	**162**
	diurnal		2118:30	2123:30	58.7	−93.93	−38.2	−24	42	4	−66
	radical		2118:30	2123:30	58.7	−93.93	−38.2	−24	60	4	−90
2	**diurnal**	**Feb 25**	**1631:30**	**1642:30**	**73.7**	**−76.00**	**−52.7**	**251**	**30**	**2**	**221**
	radical		**1631:30**	**1708:30**	**72.5**	**−78.05**	**−55.3**	**202**	**11**	**18**	**187**
	diurnal		2039:30	2039:30	59.4	−92.37	−35.8	95	57	1	38
	radical		2030:30	2039:30	59.6	−91.98	−36.8	23	13	5	7
3	**diurnal**	**March 7**	**1457:30**	**1542:30**	**65.4**	**−86.52**	**−45.7**	**151**	**22**	**12**	**124**
	radical		**1457:30**	**1542:30**	**65.4**	**−86.52**	**−45.7**	**154**	**28**	**19**	**129**
4	radical	March 21	1331:30	1522:30	68.3	−89.91	−49.4	47	30	18	7
	diurnal		1439:30	1514:30	68.5	−89.83	−49.9	21	36	6	−15
	radical	March 23	1731:30	1745:30	83.4	−61.50	−52.9	35	16	9	15
	radical	**March 24**	**1748:30**	**1801:30**	**68.2**	**−89.94**	**−51.9**	**198**	**19**	**12**	**179**
	diurnal		**1752:30**	**1801:30**	**68.1**	**−90.00**	**−51.8**	**186**	**19**	**9**	**166**
6	diurnal	April 25	1357:30	1414:30	67.7	−89.84	−43.2	7	31	10	−20
	radical		1357:30	1414:30	67.7	−89.84	−43.2	7	22	10	−17
	diurnal	April 27	1351:30	1418:30	83.0	−62.39	−45.8	111	43	16	59
	radical		1351:30	1418:30	83.0	−62.39	−45.8	111	31	16	77
	diurnal	April 28	1526:30	1547:30	71.5	−71.69	−45.4	−21	31	13	−53
	radical		1526:30	1547:30	71.5	−71.69	−45.4	−21	26	13	−38
	diurnal		1755:30	1758:30	63.9	−82.61	−45.7	4	31	2	−27
	radical		1755:30	1758:30	63.9	−82.61	−45.7	4	22	2	−18
7	diurnal	May 18	1349:30	1421:30	67.3	−90.00	−46.6	21	30	10	−9
	radical		1349:30	1421:30	67.3	−90.00	−46.6	20	21	19	−2
	diurnal	May 19	1335:30	1401:30	83.6	−61.69	−42.4	43	35	15	14
	radical		1335:30	1401:30	83.6	−61.69	−42.4	51	24	16	28
	diurnal	22 May	1536:30	1548:30	69.2	−76.06	−44.7	65	18	7	46
	radical		1536:30	1548:30	69.2	−76.06	−44.7	60	11	8	46

[a]Each row is comprised of a continuous time period within which there are measurement–model comparisons and which satisfy the altitude and latitude conditions above. Values for latitude in °N (Lat), longitude in °(Long), ambient temperature in °C (T), ambient measurement (Meas), model, and measurement–model (Meas – Model) are median values. All concentrations, including the (measurement–model) difference are in pptv. The (measurement–model) difference is calculated on a point-by-point basis and in some cases differs from the difference between the median measured and the modeled values. Model values are calculated by the diurnal steady state model and by the radical steady state model. In some cases, the time periods are exactly the same for the two models, while in other cases they differ. The two times (HHMM:SS) reflect the universal midtime for the start and end of the measurement period in each row. For emphasis, flight legs with large measurement–model discrepancies are in boldface.

second to fifth deployments of the high-latitude and 6–8 km altitude bins, in particular, show the coldest temperatures of the entire study. Many flight legs during these same extremely cold periods are the very same ones that produced the largest model underpredictions in Figure 5 and Table 3.

6.1. Temperature Dependence of the (Measurement–Model) Discrepancy for Background Air Masses

[45] The background data shown in the inset of Figure 8 for temperatures <−45°C clearly show a measurement–model bias. Although the data are limited in number (N = 32), 66% of the comparison points lie outside of the 2σ combined uncertainty limits. We obtain additional comparison points (N = 73) in this temperature regime by using the radical steady state model and slightly relaxed background parsing criteria based on the more abundant measurements of NO, NO_x, NO_y, and CNC. In Figure 9, we plot the (measurement–model) CH_2O difference as a function of ambient temperature. In addition to the original parsed data we also plot the bin average, median, and standard deviation for the difference, which are calculated for each 2°C temperature range and an exponential fit of the bin averages. This fit is only to facilitate the observation of the temperature trend and not meant to convey the functional form of the discrepancy.

[46] As can be seen by the original data, and more clearly by the temperature-binned data, the (measurement–model) comparisons show a clear departure from 0, starting at temperatures below −45°C, the same temperature range persistent for the high-latitude and high-altitude measurement–model comparisons of deployments 2–5. For facility of discussion we refer to this temperature region as the "very low temperature region." This region spans different flights and different times. The nonparsed full data set shows this same trend only with additional scatter. The average and median (measurement–model) discrepancy in this region are 127 ± 107 and 132 pptv, respectively, with maximum and minimum values of 392 and −70 pptv, respectively. The corresponding comparisons with the diurnal steady state model produce similar results with about one-half the number of points: average and median differences of 113 ± 115 and 126 pptv, respectively, are calculated. By contrast, at temperatures warmer than −45°C in Figure 9, the binned measurements and radical steady state model results are in excellent agreement: one calculates an average difference of 7 ± 71 pptv and a median difference of

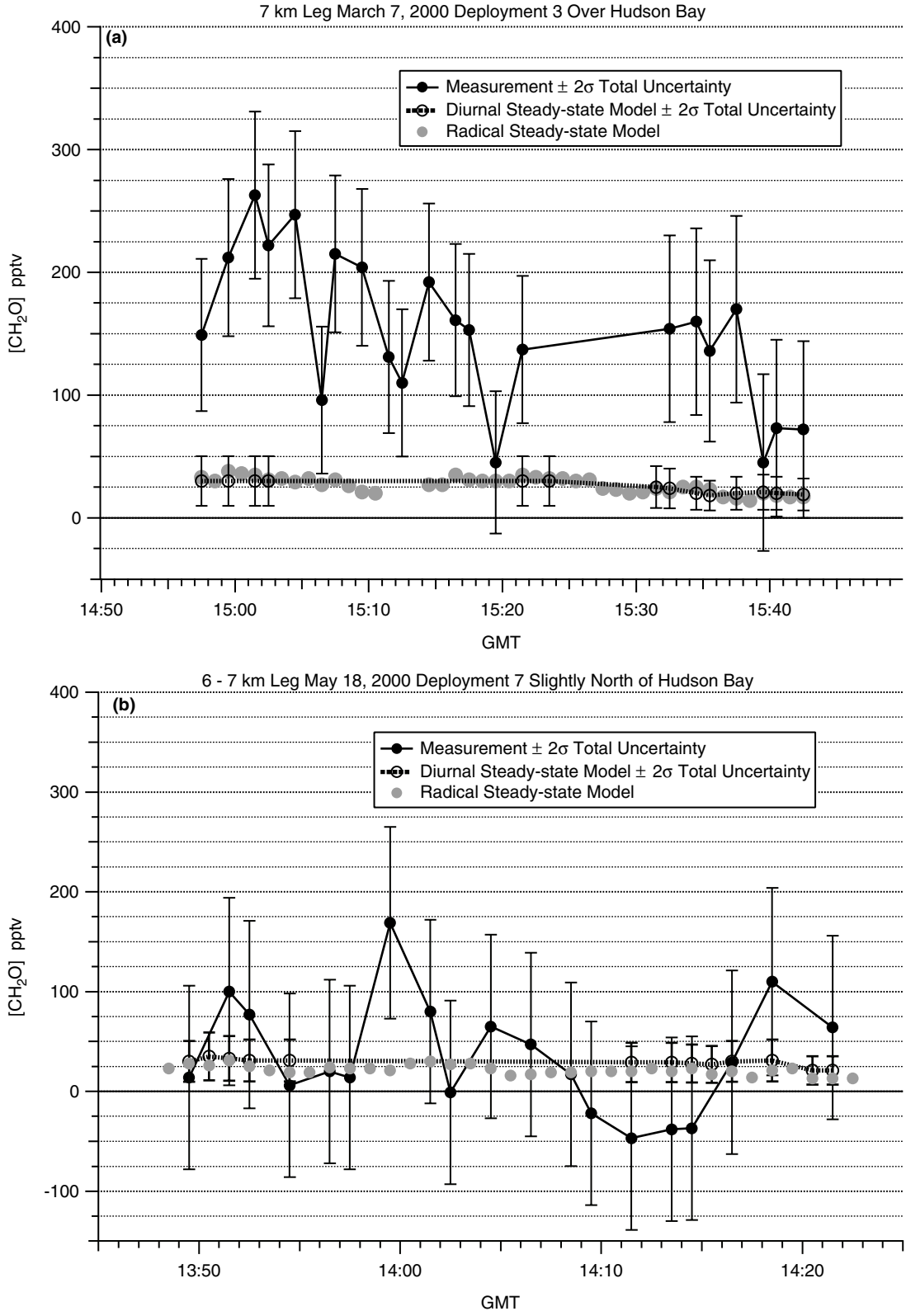

Figure 7. (a) Measured and modeled high-altitude (7 km) time series plots acquired on 7 March in deployment 3. The total uncertainties for both measurements and models at the 2σ level are shown by the error bars. (b) Similar plot as (a) but only for 18 May in the seventh deployment. The median temperature for the entire time series is −45.7°C in (a) and −46.6°C in (b).

Table 4. Background Selection Criteria Beyond Which the Air Mass in Question was Eliminated From Consideration[a]

Species	Cutoff Limit
O_3	≤37 ppbv
NO	≥28 pptv
NO_x	≥60 pptv
NO_y	≥568 pptv
CO (canister measurements)	≥162 ppbv
C_2Cl_4	≥9.5 pptv
NMHC Sum	≥3204 pptv
Alkene Sum	≥40 pptv
Benzene	≥135 pptv
CNC	≥600 particles cm^{-3}

[a]In all but three cases (NMHC sum, alkene sum, and CNC), the background cutoff limits represent the upper 10% concentration for the species in question. The three exceptions use the upper 20% concentration limit.

−1 pptv. Corresponding comparisons with the diurnal steady state model produce similar results: average and median differences of 3 ± 69 and −6 pptv, respectively. The large outlier points of Figure 9 at temperatures >−45°C are few in number compared to the bulk of the comparisons near 0 difference. In contrast, the very low temperature points of Figure 9 have very few small and negative deviations. At the highest temperature bin in Figure 9, the average (−61 pptv) and median (−65 pptv) (measurement−model) discrepancies are somewhat larger than the rest of the warmer region (T > −45°C). This may be an artifact caused by the low number of binned points (N = 5). The average number of binned points for the entire warm region is 28 and 13 for the very low temperature region.

[47] As seen in Table 3, which comprises a subset of the broader altitude and latitude comparison points of Figure 9, very low temperatures were encountered on every deployment; however, these temperatures were more persistent in deployments 2−5. It is important to reiterate that the very low temperature region did not experience recent anthropogenic emissions: the median concentrations of NO, NO_x, NO_y, and CNC were 12 pptv, 29 pptv, 367 pptv, and 125 particles cm^{-3}, respectively. The measurement precision for comparisons in the very low temperature regime, moreover, should not be an issue. Like Figure 7a, which comprises one flight leg in this regime, the measurement precision (median 2σ precision = 76 pptv) is smaller than the (measurement−model) difference. When one further combines this with measurement and model uncertainty estimates (2σ levels) in quadrature, one arrives at a median total uncertainty of 79 pptv for the (measurement−model) difference of Figure 9. By comparison, 50% of the (measurement−model) differences yield values greater than 132 pptv and 25% yield differences larger than 191 pptv for the very low temperature regime.

[48] Although there are time periods where the measurements and models are in agreement at very low temperatures (see Figure 9 and Table 3), the model underestimates the measurements for the majority of points (66%), at least for the first 4 deployments. By contrast, during the sixth and seventh deployments, virtually all the very low temperature comparisons yield measurement−model agreement within the mutual uncertainties. Figure 7b is a case in point. At time periods extending from 1354 to 1418 GMT, the ambient temperature was less than −45°C, yet with the exception of the 1 point at 1400 GMT, the measured and modeled CH_2O concentrations are in excellent agreement. Thus, very low temperatures appear to be a necessary but not sufficient condition for large (measurement−model) discrepancies in background air masses. Perhaps low light conditions as well as cold temperatures may be important in this regard. The CH_2O lifetime, which is largely controlled by CH_2O photolysis, averages 5.7 hours in Figure 7a (average solar zenith angle for this deployment was 76°), compared to 2.3 hours in Figure 7b (average solar zenith for

Table 5a. Tabulation of All Background 1-min CH_2O Measurements and Model Results in Three Latitude and Five Altitude Bins for All Six Deployments Combined[a]

Lat Bin	Palt Bin, km	Measurement Mean ± 1σ	Measurement Median	N	Model Median
40−50°N	0−0.2	–	–	–	–
	0.2−2	–	–	–	–
	2−4	87 ± 67	74	18	122
	4−6	76 ± 69	58	80	61
	6−8	64 ± 79	52	60	49
50−57°N	0−0.2	–	–	–	–
	0.2−2	105 ± 18	105	2	203
	2−4	38 ± 55	28	13	66
	4−6	55 ± 54	53	51	61
	6−8	71 ± 91	42	72	44
>57°N	0−0.2	110 ± 59	110	22	81
	0.2−2	97 ± 105	82	60	72
	2−4	72 ± 70	61	82	61
	4−6	40 ± 58	31	236	35
	6−8	63 ± 92	28	47	30

[a]Measurements and model results are given in pptv. The parsing criteria of Table 4 were used to generate these data. This table is the analog of Table 2a where all the measured and modeled CH_2O values are tabulated.

Table 5b. Tabulation of All Background 1-min Point-to-Point CH_2O (Measurement−Model) Differences in Three Latitude and Five Altitude Bins for All Six Deployments Dombined[a]

Lat Bin	Palt Bin, Km	Mean Diff. ± 1σ	Median Diff.	N	Diff. Range
40−50°N	0−0.2	–	–	–	–
	0.2−2	–	–	–	–
	2−4	−39 ± 63	−48	18	−142 to 76
	4−6	8 ± 63	2	80	−107 to 153
	6−8	7 ± 79	−4	60	−112 to 388
50−57°N	0−0.2	–	–	–	–
	0.2−2	−97 ± 18	−97	2	−110 to −84
	2−4	−26 ± 54	−23	13	−122 to 78
	4−6	−9 ± 49	−13	51	−124 to 97
	6−8	25 ± 96	7	72	−109 to 276
>57°N	0−0.2	33 ± 64	33	22	−94 to 157
	0.2−2	18 ± 110	1	60	−162 to 450
	2−4	12 ± 69	10	82	−133 to 253
	4−6	2 ± 57	−6	236	−116 to 226
	6−8	33 ± 95	6	47	−91 to 391

[a]Differences (Diff.) are given in pptv. Note that the median point-to-point differences here are slightly different than the differences of the median values shown in Table 5a. This table is the analog of Table 2b where all the measured and modeled CH_2O values are compared.

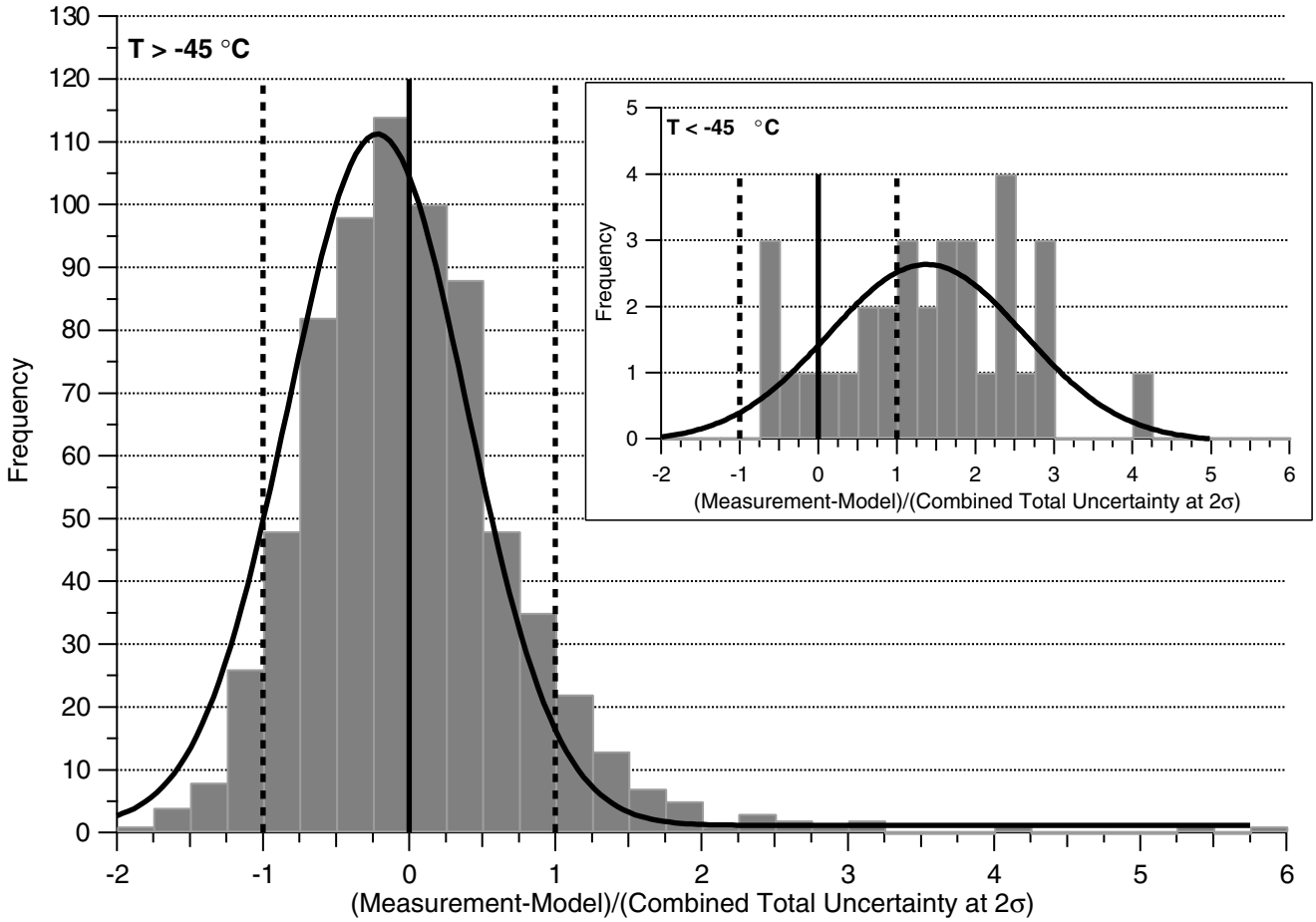

Figure 8. Histogram for the (measurement − base case model) difference normalized by the combined total measurement and model uncertainty (2σ level) for the 711 background conditions defined in Table 4 where the ambient temperature is greater than −45°C and the 32 points where the temperature <−45°C in the inset. The dark solid lines show the Gaussian fits.

this deployment was 58°). However, additional factors may be important, as the photolysis rates for the CH_2O measurement–model agreement times at 1506 and 1519 GMT in Figure 7a are within 14% of those for the full profile of Figure 7a.

6.2. Possible Mechanisms Responsible for the Very Low Temperature (Measurement–Model) Discrepancy and the Effect on Upper Tropospheric HO_x Budget

[49] In a number of recent studies, model CH_2O calculations were consistently lower than clean background ambient measurements [*Ayers et al.*, 1997; *Weller et al.*, 2000; *Jaeglé et al.*, 2000; *Frost et al.*, 2002], and in some cases this has fueled speculation concerning the need for additional CH_2O production mechanisms. In this section, we examine the measurement–model agreement using the radical steady state calculation employing various hypothetical new CH_2O production mechanisms.

[50] Recent CH_2O measurement–model comparisons [*Ayers et al.*, 1997; *Weller et al.*, 2000] as well as laboratory studies [*Elrod et al.*, 2001] have speculated on the direct production of CH_2O from the following reaction:

(R5) $\quad CH_3O_2 + HO_2 \rightarrow CH_2O + H_2O + O_2.$

Table 6. Median Ambient Temperatures (T, °C) as a Function of Latitude Bin (Lat Bin), Altitude Bin (Palt Bin, km), and Deployment Number When CH_2O Measurements (Not Parsed for Background Conditions) and Model Values are Present[a]

Lat Bin	Deployment	Palt Bin	Median T	Palt Bin	Median T
40–50°N	1	**4–6**	−22.0	**6–8**	−38.6
	2		−22.7		
	3		−21.5		−33.9
	4		−23.8		−35.7
	5				
	6		−18.2		−33.3
	7		−10.5		−26.0
50–57°N	1	**4–6**	−29.0	**6–8**	−36.0
	2		−28.6		−39.3
	3		−18.1		−33.7
	4		−25.6		−43.9
	5				
	6		−20.4		−35.3
	7		−27.9		−30.9
>57°N	1	**4–6**	−29.6	**6–8**	−38.2
	2		−32.9		**−50.3**
	3		−28.2		**−45.2**
	4		−33.9		**−50.9**
	5		−32.7		**−49.7**
	6		−32.3		−44.6
	7		−30.5		−43.0

[a]Temperatures in boldface are lower than −45°C.

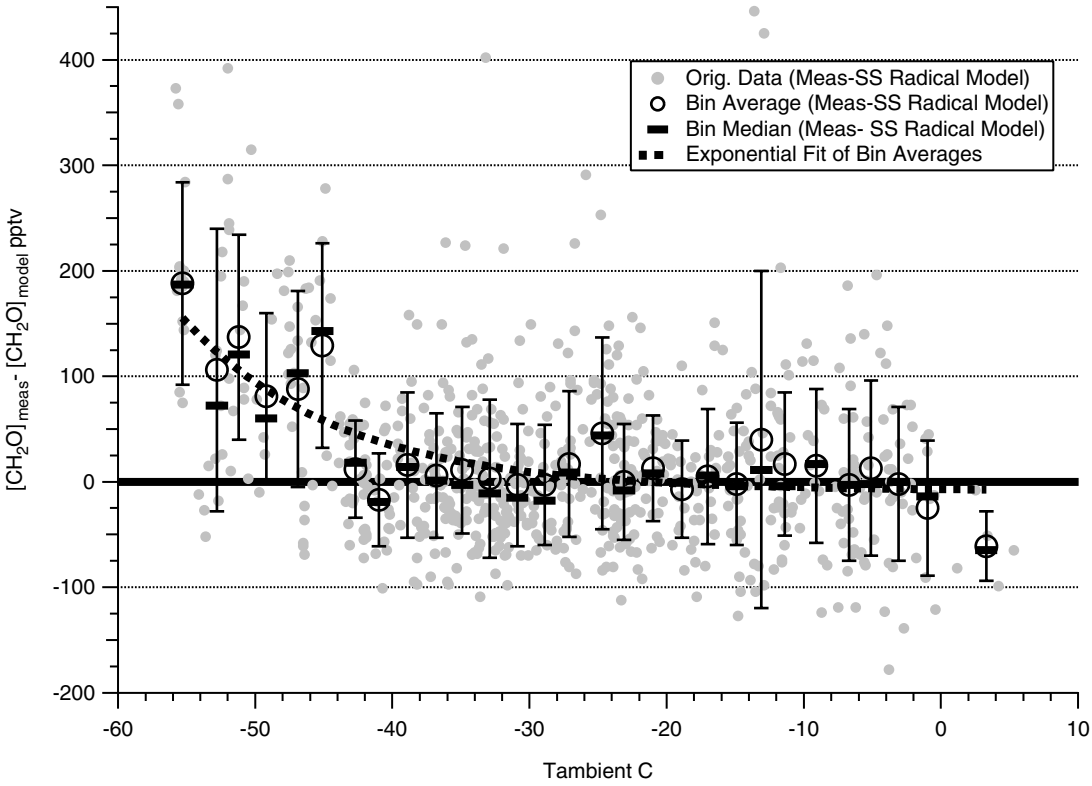

Figure 9. CH_2O (measurement−model) differences versus ambient sampling temperature for background conditions based on the fast measurements of NO, NO_x, NO_y, and CNC. The comparisons for both original background data and bin averages (2°C temperature bins) are shown. The dashed line is an exponential fit of the bin averages. The number of points in each bin ranges between an average of 13 for temperatures <−45°C and 28 for warmer temperatures.

This reaction, which is not included in most standard models, including the two employed in this study, may accelerate the production of CH_2O by circumventing the production of CH_3OOH via (R6), which is included in models:

$$\text{(R6)} \qquad CH_3O_2 + HO_2 \rightarrow CH_3OOH + O_2$$

Despite the fact that CH_3OOH photolysis and reaction with OH will also produce CH_2O, inclusion of (R5) will accelerate the CH_2O production rate when $[CH_3OOH]$ is fixed by the measurements.

[51] During clean marine low NO_x background conditions at Cape Grim, *Ayers et al.* [1997] measured hourly CH_2O averages that were consistently higher by about a factor of 2 than those modeled using a standard set of reactions ((R5) yield set to 0). This discrepancy was eliminated when a temperature-independent branching ratio of 0.40 was assumed for (R5) and 0.60 for (R6). Following the work of Ayers et al., *Weller et al.* [2000] included (R5) with a branching ratio of 0.40 in their calculations and found much better measurement−model agreement. Very recently, *Elrod et al.* [2001] studied the kinetics of (R5) and (R6) as a function of temperature (298−218 K) in a turbulent flow tube and found that the reaction rate and branching ratio for (R5) increased as the temperature decreased. The branching ratio increased from 0.11 at 25°C to 0.31 at temperatures around −55°C. Based on photochemical model and ground-based measurement comparisons in the urban Nashville plume, *Thornton et al.* [2002] have concluded that the product of the rate constant and branching ratio for the reaction between RO_2 and HO_2 to form ROOH and O_2 needs to be reduced by a factor of 3−12. Such a reduction may lead to increased CH_2O production at higher NO concentrations.

[52] The steady state radical model was run to include each of the above cases as well as one additional case involving the production and destruction of the stable reservoir species CH_3OONO_2 (MPN). The companion paper by *Cantrell et al.* [2003] gives details of these calculations and the input assumptions. The formation of MPN, which becomes more favorable as the temperature is lowered, results from the association of CH_3O_2 with NO_2. Thermal decomposition will reform the starting materials. However, by analogy to HO_2NO_2, photolysis could produce $CH_3O + NO_3$ about 1/3 of the time. The CH_3O radical would then rapidly form CH_2O by reaction with O_2. These calculations only give a rough estimate for the importance of MPN since there are large uncertainties in the dissociation and photolysis rates, quantum yields, and whether or not MPN is in steady state.

[53] When plots analogous to Figure 9 are constructed for the various cases just described, one finds only slight improvements between measured and modeled values for the very low temperature region. The *Thornton et al.* [2002] assumption, where the rate between RO_2 and HO_2 was

reduced by a factor of 12 improves the agreement the most. However, the improvement is only 29 pptv, and, as with all the nonbase case results, this slight improvement is achieved at the expense of larger disagreement in the higher-temperature regime starting at around −10°C. These results, therefore, offer no clear indication supporting any one mechanism over the rest. In fact, one can argue that the base case provides the best overall agreement over the entire temperature range. This does not imply that the temperature-dependent (R5) yield prescribed by *Elrod et al.* [2001] is not operative, but it is not sufficient to explain the (measurement−model) discrepancies observed here.

[54] In addition to the mechanisms above, *Jaeglé et al.* [2000] raised the possibility of heterogeneous conversion of methanol to CH_2O on aerosols to explain factors of 2–3 model underpredictions during the SONEX airborne campaign in the 8–12 km range. The aerosol measurements of the present study do not show any obvious differences between the two temperature regimes with respect to aerosol size, number density, or surface area. In addition, the limited canister methanol measurements of the present study also do not reveal elevated concentrations in the low temperature regime in question. The measurements of the present study, therefore, do not reveal any obvious indicators to support heterogeneous conversion of methanol to CH_2O on aerosols as the cause of the very low temperature (measurement−model) discrepancies. This is supported by the recent laboratory study of *Iraci et al.* [2002], which found no evidence for reaction of methanol with cold sulfuric acid aerosols.

[55] Other factors that should be considered in the observed (measurement−model) discrepancies at low temperatures include reactions of $O(^1D)$ and/or Cl with CH_4, systematically high CH_2O photolysis frequencies at low temperatures, and sample inlet artifacts in the CH_2O measurements at very low temperatures. Only at altitudes greater than approximately 25 km are the concentrations of $O(^1D)$ high enough to become important in producing extra CH_2O. At temperatures around −45.6°C, Cl reaction with CH_4 is 24 times faster than OH with CH_4, and based on typical calculated [OH] around 1.2×10^5 for high altitude and high latitudes during the early deployments, Cl concentrations of only 5×10^3 mol cm^{-3} are needed to give an identical CH_2O production rate as OH. Although such concentrations might be possible for stratospheric air and indeed elevated CH_2O is sometimes observed in stratospherically influenced air as in the case of Figure 7a, enhanced CH_2O is also observed in tropospheric air in many other cases. Thus reaction of Cl with CH_4 cannot explain the elevated CH_2O in most cases. This is consistent with measurement ratios for C_2Cl_4/CH_2Cl_2 during TOPSE. Since the reaction rate of Cl with C_2Cl_4 is about a factor of 300 times that for CH_2Cl_2 and both have comparable loss rates with OH and comparable sources, one would expect to observe a sharp change in the above ratio for air in which Cl processing is prevalent. Unfortunately, there is no such clear and consistent signature with the elevated CH_2O observed during TOPSE. Likewise, based upon standard additions of CH_2O standards to ambient air in the TDLAS inlet, there is no evidence for sample loss. Such losses, moreover, would reduce the (measurement−model) discrepancies. These precautions, however, cannot rule out thermal decomposition of MPN or some other CH_2O precursor in the warm TDLAS inlet, producing a CH_2O artifact at low temperatures. The results of *Cantrell et al.* [2003] provide further evidence suggesting that the elevated CH_2O observations in the very low temperature regime is related to a real atmospheric process and not an inlet artifact. Measurement−model comparisons for the sum of HO_x and RO_x radicals by *Cantrell et al.* [2003] reveal a very similar temperature trend as Figure 9 when model calculated CH_2O concentrations are used. Employing measured CH_2O concentrations eliminates the very low temperature HO_x-RO_x (measurement−model) discrepancy. This observation, moreover, suggests that errors in CH_2O photolysis frequencies at low temperatures are not responsible for the CH_2O discrepancies. Although we cannot unequivocally rule out the possibility that the HO_x-RO_x measurements of *Cantrell et al.* [2003] are plagued by a similar inlet artifact as the CH_2O measurements, it is highly unlikely since all the important reagent chemistry occurs at ambient temperatures outside the aircraft cabin.

[56] Very low temperatures and elevated CH_2O concentrations at high altitudes were observed over a rather wide geographic area during TOPSE. Elevated CH_2O measurements were observed from latitudes as far south as 50.9°N over Lake Winnipeg in February to as far north as 83.7°N over the Arctic Ocean during March and April. Whatever the cause, the elevated CH_2O concentrations observed in this study may have a significant impact on upper tropospheric HO_x. For example, when one calculates the ratio of diurnally averaged HO_x employing measured CH_2O to that using modeled CH_2O, one arrives at a ratio of 1.7 for high latitudes (>57°N) and high altitudes (6–8 km) during the third deployment. This ratio extrapolates to a value of 2.2 during the first deployment and linearly drops to 1.2–1.3 during the last two deployments. The companion paper by *Cantrell et al.* [2003] discusses the HO_x budget in further detail.

[57] It is interesting to note that ER-2 measurements of HO_x by *Wennberg et al.* [1998] over California at around 8 km (solar zenith angle of 70°) are as much as a factor of 2 higher than those modeled using primary production from the reaction of $O(^1D)$ with H_2O with the addition of acetone photolysis. *Wennberg et al.* [1998] note that the biggest (measurement−model) discrepancies occurred during winter and for the highest solar zenith angles. During the first four deployments in TOPSE where elevated CH_2O was observed, the high-altitude (6–8 km), high-latitude (>57°N) solar zenith angles ranged between 82° (first deployment) and 75° (fourth deployment). Although the elevated CH_2O concentrations observed in the present study are consistent with the missing HO_x noted by *Wennberg et al.* [1998], at present it is not clear if there is a direct linkage, since no CH_2O measurements were acquired by *Wennberg et al.* [1998]. Nevertheless, the elevated high-latitude and high-altitude CH_2O observations during TOPSE illustrates the importance of CH_2O in the HO_x budget of the middle, and quite possibly upper, troposphere.

7. Summary and Conclusions

[58] The present paper describes an extensive set of 1-min airborne CH_2O measurements acquired by TDLAS during

the TOPSE study and comprehensive comparisons with steady state model calculations. Measurements were segregated into 3 latitude and 5 altitude bins, and all 3 latitude bins revealed decreasing CH_2O concentration with increasing altitude, as expected from the decreased source strength and increased photolysis rates. With the exception of the lowest latitude bin for the lowest altitudes (0.2–4 km), and the 4–8 km altitude range for the highest latitude bin, the median measured CH_2O concentrations either did not show any clear temporal trends from February to May in each altitude bin or such trends were negligibly small. The low-latitude, low-altitude exception (increasing [CH_2O] with time), was caused by increases in CH_2O boundary layer sources, and in OH, NO, and temperature. The high-latitude and high-altitude exception (decreasing [CH_2O] with time) revealed additional CH_2O sources from February to mid-April.

[59] Measurement–model comparisons were carried out using a number of different approaches using two different models. Under background conditions, which should be the most appropriate for comparison since the modeling limitations are minimized, the overall agreement ranges between −13% and +5% for temperatures warmer than −45°C. This corresponds to mean and median (measurement–model) differences of 3 ± 69 and −6 pptv, respectively. This agreement is quite good, particularly when one considers the factors of 2–3 model underpredictions in many recent studies. Although many factors may be operative in such comparisons, the results of the present study along with those from *Wagner et al.* [2002] suggest that it is indeed possible to obtain good measurement–model agreement on average under background conditions without recourse to additional CH_2O production mechanisms, at least at temperatures warmer than −45°C. At colder temperatures, significant differences were observed for deployments 2–5 (February to 4 April) over a wide geographic region from southern Canada over Lake Winnipeg to the Arctic Ocean. For background conditions, measured CH_2O was as much as 392 pptv higher than modeled, and the median difference was 132 pptv at very low temperatures. In contrast, virtually all the very low temperature comparisons produced good measurement–model agreement during deployments 6 and 7 (23 April to 23 May). Thus, very low temperatures appear to be a necessary but not sufficient condition for additional sources of CH_2O in background air masses. Perhaps low light conditions as well as cold temperatures may be important in this regard. A number of possible mechanisms were investigated, and aside from slight improvements in the agreement, the model underprediction was still large and this was achieved at the expense of poorer agreement at warmer temperatures. Thus there is no clear evidence supporting one mechanism over the rest. Numerous other possibilities were also considered, and in each case there was no compelling evidence to support any of the hypotheses. Unmeasured NMHCs cannot be ruled out as the cause of the low temperature discrepancy.

[60] Whatever the cause, the elevated CH_2O concentrations observed in this study may have a significant impact on upper tropospheric HO_x at high latitudes during the February–March time frame. Clearly, additional CH_2O measurement–model comparisons employing measurements with even higher precision than the present study are needed over a wide range of geographic regions and sampling conditions to further address the many questions raised herein. Such studies should further investigate the role of aerosol composition, air mass history, particularly chemical processing that may occur in the dark, as well as the presence of additional carbon-containing compounds not measured during TOPSE.

[61] **Acknowledgments.** The National Center for Atmospheric Research is sponsored by the National Science Foundation. The authors wish to acknowledge the Research Aviation Facility of NCAR and each of its participants for operating the C-130 aircraft under very harsh conditions. The authors also wish to acknowledge Bill Mankin at NCAR for measurements of CO during TOPSE and Anthony Wimmers and Jennie Moody at the University of Virginia for back trajectory analysis.

References

Arlander, D. W., D. Bruning, U. Schmidt, and D. H. Ehhalt, The tropospheric distribution of formaldehyde during TROPOZ II, *J. Atmos. Chem.*, *22*, 251–268, 1995.

Atkinson, R., et al., Evaluated kinetic and photochemical data for atmospheric chemistry, *J. Phys. Chem. Ref. Data*, *26*, 1329–1499, 1997.

Atlas, E., B. Ridley, and C. Cantrell, The TOPSE Experiment: Introduction, *J. Geophys. Res.*, *108*, doi:10.1029/2002JD003172, in press, 2003.

Ayers, G. P., R. W. Gillett, H. Granek, C. de Serves, and R. A. Cox, Formaldehyde production in clean marine air, *Geophys. Res. Lett.*, *24*, 401–404, 1997.

Blake, N. J., D. R. Blake, B. C. Sive, A. S. Katzenstein, S. Meinardi, O. W. Wingenter, E. L. Atlas, F. Flocke, B. A. Ridley, and F. S. Rowland, The seasonal evolution of NMHCs and light alkyl nitrates at middle to high northern latitudes during TOPSE, *J. Geophys. Res.*, *108*, doi:10.1029/2001JD001467, in press, 2003.

Brune, W. H., et al., Airborne in situ OH and HO_2 observations in the cloud-free troposphere and stratosphere during SUCCESS, *Geophys. Res. Lett.*, *25*, 1701–1704, 1998.

Calvert, J. G., R. Atkinson, J. A. Kerr, S. Madronich, G. K. Moortgat, T. J. Wallington, and G. Yarwood, *The Mechanisms of Atmospheric Oxidation of the Alkenes*, pp. 371–379, Oxford Univ. Press, New York, 2000.

Cantrell, C. A., R. E. Shetter, T. M. Gilpin, J. G. Calvert, F. L. Eisele, and D. J. Tanner, Peroxy radical concentrations measured and calculated from trace gas measurements in the Mauna Loa Observatory Photochemistry Experiment 2, *J. Geophys. Res.*, *101*, 14,653–14,664, 1996.

Cantrell, C. A., et al., Peroxy radical behavior during the winter-to-spring seasonal transition at middle to high latitudes during TOPSE, *J. Geophys. Res.*, *108*, doi:10.1029/2002JD002715, in press, 2003.

Crawford, J. H., et al., Implications of large scale shifts in tropospheric NO_x levels in the remote tropical Pacific, *J. Geophys. Res.*, *102*, 28,447–28,468, 1997.

Crawford, J. H., et al., Assessment of upper tropospheric HO_x sources over the tropical Pacific based on NASA GTE/PEM data: Net effect on HO_x and other photochemical parameters, *J. Geophys. Res.*, *104*, 16,255–16,273, 1999.

Davis, D. D., et al., Assessment of the ozone photochemistry tendency in the western North Pacific as inferred from PEM-West A observations during the fall of 1991, *J. Geophys. Res.*, *101*, 2111–2134, 1996.

Davis, D. D., et al., Marine latitude/altitude OH distributions: Comparison of Pacific Ocean observations with models, *J. Geophys. Res.*, *106*(D23), 32,691–32,707, 2001.

DeMore, W. B., et al., Chemical kinetics and photochemical data for use in stratospheric modeling, *JPL Publ.*, vol. 97-4, 266 pp., 1997.

deServes, C., Gas phase formaldehyde and peroxide measurements in the Arctic atmosphere, *J. Geophys. Res.*, *99*, 25,391–25,398, 1994.

Elrod, M. J., D. L. Ranschaert, and N. J. Schneider, Direct kinetics study of the temperature dependence of the CH_2O branching channel for the $CH_3O_2 + HO_2$ reaction, *Int. J. Chem. Kinet.*, *33*, 363–376, 2001.

Fried, A., S. Sewell, B. Henry, B. P. Wert, and J. R. Drummond, Ground-based tunable diode laser measurements of formaldehyde: Improvements in system performance and recent field campaigns, *SPIE Proc.*, *2834*, 160–174, 1996.

Fried, A., S. Sewell, B. Henry, B. P. Wert, T. Gilpin, and J. R. Drummond, Tunable diode laser absorption spectrometer for ground-based measurements of formaldehyde, *J. Geophys. Res.*, *102*, 6253–6266, 1997a.

Fried, A., et al., Photochemistry of formaldehyde during the 1993 tropospheric OH photochemistry experiment, *J. Geophys. Res.*, *102*, 6283–6296, 1997b.

Fried, A., B. Henry, B. Wert, S. Sewell, and J. R. Drummond, Laboratory, ground-based, and airborne tunable diode laser systems: Performance characteristics and applications in atmospheric studies, *Appl. Phys. B*, *67*, 317–330, 1998a.

Fried, A., B. P. Wert, B. Henry, and J. R. Drummond, Airborne tunable diode laser measurements of trace atmospheric gases, *SPIE Proc.*, *3285*, 154–162, 1998b.

Fried, A., B. Wert, B. Henry, J. R. Drummond, G. Frost, and Y.-N. Lee, Airborne tunable diode laser measurements of formaldehyde during the 1997 North Atlantic Regional Experiment, *SPIE Proc.*, *3758*, 90–99, 1999.

Fried, A., Y.-N. Lee, G. Frost, B. Wert, B. Henry, J. R. Drummond, G. Hubler, and T. Jobson, Airborne CH_2O measurements over the North Atlantic during the 1997 NARE campaign: Instrument comparisons and distributions, *J. Geophys. Res.*, *107*(D12), 4039, doi:10.1029/2000JD000722, 2002.

Frost, G. J., et al., Comparison of box model calculations and measurements of formaldehyde from the 1997 North Atlantic Regional Experiment, *J. Geophys. Res.*, *107*(D12), 4060, doi:10.1029/2001JD000896, 2002.

Gilpin, T., et al., Intercomparison of six ambient [CH_2O] measurement techniques, *J. Geophys. Res.*, *102*, 21,161–21,188, 1997.

Harder, J. W., A. Fried, S. Sewell, and B. Henry, Comparison of tunable diode laser and long path ultraviolet/visible spectroscopic measurements of ambient formaldehyde concentrations during the 1993 OH photochemistry experiment, *J. Geophys. Res.*, *102*, 6267–6282, 1997.

Iraci, L. T., A. M. Essin, and D. M. Golden, Solubility of methanol in low-temperature aqueous sulfuric acid and implications for atmospheric particle composition, *J. Phys. Chem. A*, *106*, 4054–4060, 2002.

Jaeglé, L., et al., Observed OH and HO_2 in the upper troposphere suggest a major source from convective injection of peroxides, *Geophys. Res. Lett.*, *24*, 3181–3184, 1997.

Jaeglé, L., D. J. Jacob, W. H. Brune, D. Tan, I. C. Faloona, A. J. Weinheimer, B. A. Ridley, T. L. Campos, and G. W. Sachse, Sources of HO_x and production of ozone in the upper troposphere over the United States, *Geophys. Res. Lett.*, *25*, 1709–1712, 1998.

Jaeglé, L., et al., Photochemistry of HO_x in the upper troposphere at northern midlatitudes, *J. Geophys. Res.*, *105*, 3877–3892, 2000.

Liu, S. C., et al., A study of the photochemistry and ozone budget during the Mauna Loa Observatory Photochemistry Experiment, *J. Geophys. Res.*, *97*, 10,463–10,471, 1992.

McKeen, S. A., T. Gierczak, J. B. Burkholder, P. O. Wennberg, T. F. Hanisco, E. R. Keim, R.-S. Gao, S. C. Liu, A. R. Ravishankara, and D. W. Fahey, The photochemistry of acetone in the upper troposphere: A source of odd-hydrogen radicals, *Geophys. Res. Lett.*, *24*, 3177–3180, 1997.

Neri, F., G. Saitta, and S. Chiofalo, An accurate and straightforward approach to line regression analysis of error-affected experimental data, *J. Phys. E Sci. Instrum.*, *22*, 215–217, 1989.

Prather, M. J., and D. J. Jacob, A persistent imbalance in HO_x and NO_x photochemistry of the upper troposphere driven by deep tropical convection, *Geophys. Res. Lett.*, *24*, 3189–3192, 1997.

Ridley, B., et al., Ozone depletion events observed in the high latitude surface layer during the TOPSE aircraft program, *J. Geophys. Res.*, *108*(D4), 8356, doi:10.1029/2001JD001507, 2003.

Sander, S. P., et al., Chemical kinetics and photochemical data for use in stratospheric modeling, evaluation number, *JPL Publ.*, vol. 13, 00-3, 2000.

Sewell, S., A. Fried, B. Henry, and J. R. Drummond, A field diode laser spectrometer employing an astigmatic Herriott cell, *SPIE Proc.*, *2112*, 72–80, 1993.

Shepson, P. B., A.-P. Sirju, J. F. Hopper, L. A. Barrie, V. Young, H. Niki, and H. Dryfhout, Sources and sinks of carbonyl compounds in the Arctic Ocean boundary layer: A polar icefloe experiment, *J. Geophys. Res.*, *101*, 21,081–21,089, 1996.

Singh, H., et al., High concentrations and photochemical fate of oxygenated hydrocarbons in the global troposphere, *Nature*, *378*, 50–54, 1995.

Sumner, A. L., and P. B. Shepson, Snowpack production of formaldehyde and its effect on the Arctic troposphere, *Nature*, *398*, 230–233, 1999.

Sumner, A. L., P. B. Shepson, A. M. Grannas, J. W. bottenheim, K. G. Anlauf, D. Worthy, W. H. Schroeder, A. Steffen, F. Domine, S. Perrier, and S. Houdier, Atmospheric chemistry of formaldehyde in the Arctic troposphere at polar sunrise, and the influence of the snowpack, *Atmos. Environ.*, *36*, 2553–2562, 2002.

Thornton, J. A., et al., Observations of ozone production rates as a function of NO_x abundances and HO_x production rates in the Nashville urban plume, *J. Geophys. Res.*, *107*(D12), 4146, doi:10.1029/2001JD000932, 2002.

Wagner, V., R. von Glascow, H. Fischer, and P. J. Crutzen, Are CH_2O measurements in the marine boundary layer suitable for testing the current understanding of CH_4 photooxidation?, *J. Geophys. Res.*, *107*(D3), 4029, doi:10.1029/2001JD000722, 2002.

Wang, Y., et al., Springtime photochemistry at northern middle and high latitudes, *J. Geophys. Res.*, *108*, doi:10.1029/2002JD002227, in press, 2003.

Weller, R., O. Schrems, A. Boddenberg, S. Gab, and M. Gautrois, Meridional distribution of hydrogen peroxides and formaldehyde in the marine boundary layer of the Atlantic (48°N–35°S) measured during the Albatross campaign, *J. Geophys. Res.*, *105*, 14,401–14,412, 2000.

Wennberg, P. O., et al., Hydrogen radicals, nitrogen radicals, and the production of O_3 in the upper troposphere, *Science*, *279*, 49–53, 1998.

Wert, B. P., A. Fried, B. Henry, and J. R. Drummond, Airborne measurements of tropospheric formaldehyde by tunable diode laser absorption spectroscopy, *SPIE Proc.*, *2834*, 175–186, 1996.

Wert, B. P., A. Fried, B. Henry, and J. R. Drummond, Enhancement of a tunable diode laser tropospheric trace gas measurement system, *SPIE Proc.*, *3758*, 100–108, 1999.

Wert, B. P., A. Fried, B. Henry, and S. Cartier, Evaluation of inlets used for the airborne measurement of formaldehyde, *J. Geophys. Res.*, *107*(D13), 4163, doi:10.1029/2001JD001072, 2002.

Zhou, X., Y.-N. Lee, L. Newman, X. Chen, and K. Mopper, Tropospheric formaldehyde concentration at the Mauna Loa Observatory during the Mauna Loa Observatory Photochemistry Experiment 2, *J. Geophys. Res.*, *101*, 14,711–14,719, 1996.

E. Atlas, C. Cantrell, M. T. Coffey, A. Fried, J. Hannigan, B. Lefer, B. Ridley, R. Shetter, J. Walega, and B. Wert, Atmospheric Chemistry Division, National Center for Atmospheric Research, Boulder, CO 80303, USA. (fried@acd.ucar.edu)

D. Blake, N. Blake, and S. Meinardi, Department of Chemistry, University of California, Irvine, 516 Rowland Hall, Irvine, CA 92697, USA.

J. Dibb, E. Scheuer, and B. Talbot, Institute for the Study of Earth, Oceans, and Space, University of New Hampshire, Morse Hall, 39 College Road, Durham, NC 03824, USA.

D. Ehhalt, Institute for Atmospheric Chemistry, Leo-Brandt-Strasse, D-52428 Julich, Germany.

B. Heikes and J. Snow, School of Oceanography, University of Rhode Island, South Ferry Road, Narragansett, RI 02882, USA.

Y. Wang, Earth and Atmospheric Sciences Department, Georgia Institute of Technology, 221 Bobby Dodd Way, Atlanta, GA 30332-0340, USA.

O. Wingenter, Department of Chemistry, New Mexico Institute of Mining and Technology, Socorro, NM 87801, USA.